Astronomy & Astrophysics manuscript no. sn2011dh-2-aa-resubmit-v4
October 24, 2014

The Type IIb SN 2011dh - 2 years of observations and modelling of the lightcurves.

M. Ergon[1], A. Jerkstrand[2], J. Sollerman[1], N. Elias-Rosa[3], C. Fransson[1], M. Fraser[4,2], A. Pastorello[3], R. Kotak[2], S. Taubenberger[5], L. Tomasella[3], S. Valenti[6,7], S. Benetti[3], G. Helou[8], M.M. Kasliwal[9], J. Maund[2], S.J. Smartt[2], and J. Spyromilio[10]

[1] The Oskar Klein Centre, Department of Astronomy, AlbaNova, Stockholm University, 106 91 Stockholm, Sweden
[2] Astrophysics Research Centre, School of Mathematics and Physics, Queens University Belfast, Belfast, BT7 1NN, UK
[3] INAF, Osservatorio Astronomico di Padova, vicolo dell'Osservatorio n. 5, 35122 Padua, Italy
[4] Institute of Astronomy, University of Cambridge, Madingley Road, Cambridge, CB3 0HA
[5] Max-Planck-Institut für Astrophysik, Karl-Schwarzschild-Str. 1, D-85741 Garching, Germany
[6] Las Cumbres Observatory Global Telescope Network, 6740 Cortona Dr., Suite 102, Goleta, CA 93117, USA
[7] Department of Physics, University of California, Santa Barbara, Broida Hall, Mail Code 9530, Santa Barbara, CA 93106-9530, USA
[8] Infrared Processing and Analysis Center, California Institute of Technology, Pasadena, CA 91125, USA
[9] Observatories of the Carnegie Institution for Science, 813 Santa Barbara St, Pasadena, CA 91101, USA
[10] ESO, Karl-Schwarzschild-Strasse 2, 85748 Garching, Germany

Submitted to Astronomy and Astrophysics

ABSTRACT

We present optical and near-infrared (NIR) photometry and spectroscopy as well as modelling of the lightcurves of the Type IIb supernova (SN) 2011dh. Our extensive dataset, for which we here present the post 100 days observations, spans 2 years, and complemented with Spitzer mid-infrared (MIR) data, we use it to build a 3−732 days optical-to-MIR bolometric lightcurve. To model the <400 days bolometric lightcurve we use a hydrodynamical model grid, which allows us to determine the errors in the derived quantities, and a bolometric correction determined with steady-state NLTE modelling. Using this method we find a helium core mass of $3.1^{+0.7}_{-0.4}$ $M_{\odot}$ for SN 2011dh, consistent within error bars with previous results obtained using the <80 days bolometric lightcurve. We present 100−500 days bolometric and broad-band lightcurves for the Jerkstrand et al. (2014) steady-state NLTE models. The preferred 12 $M_{\odot}$ (initial mass) model, presented and found to give a good agreement with observed nebular spectra in Jerkstrand et al. (2014), shows a good overall agreement with the observed lightcurves, although some discrepancies exist. Time-dependent NLTE modelling shows that after ∼600 days a steady-state assumption is no longer valid. The radioactive energy deposition in this phase is likely dominated by the positrons emitted in the decay of ^{56}Co, but seems insufficient to reproduce the lightcurves, and what energy source is dominating the emitted flux is unclear. We find an excess in the *K* and the MIR bands developing between 100 and 250 days, during which an increase in the optical decline rate is also observed. A local origin of the excess is suggested by the depth of the He I 20581 Å absorption. Steady-state NLTE models with a modest dust opacity in the core (τ = 0.44), turned on during this period, reproduce the observed behaviour, but an additional excess in the Spitzer 4.5 μm band remains. CO first-overtone band emission is detected at 206 days, and possibly at 89 days, and assuming the additional excess to be dominated by CO fundamental band emission, we find fundamental to first-overtone band ratios considerably higher than observed in SN 1987A. The profiles of the [O I] 6300 Å and Mg I] 4571 Å lines show a remarkable similarity, suggesting these lines to originate mainly from the O/Ne/Mg zone, and using small scale fluctuations in the line profiles we estimate a filling factor of $\lesssim$0.07 for the emitting material. This paper concludes our extensive observational and modelling work on SN 2011dh. The results from hydrodynamical modelling, steady-state NLTE modelling and stellar evolutionary progenitor analysis are all consistent, and suggest an initial mass of ∼12 $M_{\odot}$ for the progenitor.

Key words. supernovae: general — supernovae: individual (SN 2011dh) — supernovae: individual (SN 1993J) — supernovae: individual (SN 2008ax) — galaxies: individual (M51)

1. Introduction

Type IIb supernovae (SNe) are observationally characterized by a transition from Type II (with hydrogen lines) at early times to Type Ib (without hydrogen lines but with helium lines) at later times. The physical interpretation is that these SNe arise from stars that have lost most of their hydrogen envelope, either through stellar winds or interaction with a binary companion. Which of these production channels dominates is still debated but for SN 1993J, the prime example of such a SN, a companion star was detected by direct observations (Maund et al. 2004; Fox et al. 2014). The evolution of this binary system has been successfully modelled (Podsiadlowski et al. 1993; Stancliffe & Eldridge 2009), and it is widely accepted that the companion was responsible for the removal of the hydrogen envelope. Bright, nearby Type IIb SNe as 1993J, 2008ax and the recent 2011dh are essential to improve our understanding of this class. Observations of the progenitor star in pre-explosion images, a search for the companion star when the SN has faded and multi-method modelling of high quality data, all provide important clues to the nature of Type IIb SNe and their progenitor stars.

In this paper we present the post 100 days part of the extensive optical and near-infrared (NIR) dataset, covering nearly two years, that we have obtained for SN 2011dh. The first 100 days of this dataset have been presented in Ergon et al. (2014, hereafter E14). Detailed hydrodynamical modelling of the SN using those data were presented in Bersten et al. (2012, hereafter B12) and steady-state NLTE modelling of nebular spectra in Jerkstrand et al. (2014, hereafter J14). Identification and analysis of the plausible progenitor star was presented in Maund et al. (2011, hereafter M11), and confirmation of the progenitor identification through its disappearance in E14.

SN 2011dh was discovered on 2011 May 31.893 UT (Griga et al. 2011; Arcavi et al. 2011) in the nearby galaxy M51, and has been extensively monitored from X-ray to radio wavelengths. Most observations cover the 3−100 days period, but late-time data have been published by Tsvetkov et al. (2012), Van Dyk et al. (2013), Sahu et al. (2013), Shivvers et al. (2013) and Helou et al. (2013). The explosion epoch (May 31.5 UT), the distance to M51 ($7.8^{+1.1}_{-0.9}$ Mpc) and the interstellar line-of-sight extinction towards the SN ($E(B\text{-}V)$=$0.07^{+0.07}_{-0.04}$ mag), are all adopted from E14. The phase of the SN is expressed relative to this explosion epoch throughout the paper.

The nature of the progenitor star has been a key issue since the identification of a yellow supergiant in pre-explosion images, coincident with the SN (M11; Van Dyk et al. 2011). Recent progress in modelling of the SN (B12; J14; Shivvers et al. 2013), and the disappearance of the progenitor candidate (E14; Van Dyk et al. 2013), strengthens the hypothesis that the progenitor was a yellow supergiant of moderate mass, as was originally proposed in M11. As shown in Benvenuto et al. (2013), a binary interaction scenario that reproduces the observed and modelled properties of the yellow supergiant is possible.

The paper is organized as follows. In Sect. 2 and 3 we present and analyse our photometric and spectroscopic observations, respectively, and compare these to SNe 1993J and 2008ax. In Sect. 4 we model the <500 days lightcurves and in Sect. 5 we discuss the >500 days lightcurves. Finally, we conclude and summarize our results in Sect. 6.

2. Photometry

Here we present observations spanning 100−732 days in the optical, 100−380 days in the NIR and 100−1061 days in the MIR, and provide analysis and comparisons with SNe 1993J and 2008ax. The distance, extinction and photometric data used for SNe 1993J and 2008ax are the same as in E14. The lack of S-corrected photometry for SN 1993J complicates the comparison, whereas for SN 2008ax, the S-corrected Johnson-Cousins (JC) photometry by Taubenberger et al. (2011) agrees reasonably well with the JC photometry by Tsvetkov et al. (2009).

2.1. Observations

The >100 days data were obtained with the Liverpool Telescope (LT), the Nordic Optical Telescope (NOT), Telescopio Nazionale (TNG), the Calar Alto 3.5m (CA 3.5m) and 2.2m (CA 2.2m) telescopes, the Asiago 67/92cm Schmidt (AS Schmidt) and 1.82m Copernico (AS 1.82m) telescopes, the William Herschel Telescope (WHT), the Albanova Telescope[1] (AT) and the United Kingdom Infrared Telescope (UKIRT). The late-time dataset includes 61 (146 in total) and 9 (32 in total) epochs of optical and NIR imaging, respectively. Spitzer has systematically been observing SN 2011dh under program ID 70207 (PI Helou), 90240 and 10136 (PI Kasliwal). E14 and Helou et al. (2013) presented Spitzer photometry (using independent procedures) up to 85 and 625 days, respectively, and here we present observations up to 1061 days. Throughout the paper, we label the 3.6 μm and 4.5 μm bands S_1 and S_2, respectively. The reduction and calibration procedures are described in E14, and issues specifically related to the >100 days data are discussed in Appendix A.

The S-corrected optical and NIR magnitudes and their corresponding errors are listed in Tables 4, 6, and 7 and the Spitzer MIR magnitudes and their corresponding errors in Table 8. The <800 days UV, optical, NIR and MIR broad-band lightcurves, including SWIFT (E14) and S-corrected HST (Van Dyk et al. 2013) photometry, are shown in Fig. 1. We also show cubic spline fits or, when the sampling is sparse, linear interpolations, as well as extrapolations assuming a constant colour to adjacent bands. These are used in a number of calculations, where the errors in the fitted splines are estimated by the standard deviation and then propagated. The extrapolation method used makes most sense in the early phase when the spectral energy distribution (SED) is dominated by the continuum. In particular, the NIR magnitudes are extrapolated between ∼400 and ∼750 days, which introduce a considerable uncertainty.

2.2. Photometric evolution

In Fig. 2 we show absolute optical, NIR and MIR broad-band lightcurves for SNe 2011dh, 1993J and 2008ax, and in Table 1 we tabulate the tail decline rates at 100, 200 and 300 days. Most striking is the similarity between the lightcurves, except for a shift towards higher luminosities for SNe 1993J and 2008ax, the shift being larger in bluer bands and negligible in the NIR, and most pronounced for SN 2008ax. As discussed in E14, this difference could be explained by errors in the adopted extinctions.

Given the caveat that SNe 1993J and 2008ax are only partly covered in U and NIR, we find the following general trends. At 100 days the V, R and I-band decline rates are roughly twice the decay rate of ^{56}Co, and subsequently decrease towards 300 days. The U and B-band decline rates are significantly lower at 100 days, after which they approach the other optical decline rates and then evolve similarly. The J and H-band decline rates are considerably higher than the optical at 100 days, subsequently approaches those and eventually become considerably lower. For SNe 2011dh and 1993J, the K-band behaves quite differently than the other NIR bands. At 100 days the decline rate is significantly lower, but as it remains roughly constant, it subsequently approaches the other NIR decline rates and eventually becomes considerably higher. As seen in Fig. 1, the optical lightcurves of SN 2011dh flatten considerably after ∼450 days, approaching a decline rate similar to, or lower than, the decay rate of ^{56}Co.

SNe 2011dh and 1993J were also monitored in the MIR S_1 and S_2 and L (similar to S_1) bands, respectively, and for both SNe a strong excess develops between 100 and 250 days. For SN 1993J the MIR coverage ends at ∼250 days, and for SN 2011dh the subsequent evolution is fairly similar to that in the optical. After ∼400 days, a considerable flattening of the lightcurves is seen, similar to, but more pronounced than in the optical, and after ∼750 days (not shown in Fig. 1) this trend continues and the MIR lightcurves become almost flat.

[1] 1.0 m Nasmyth-Cassegrain telescope at Albanova, Stockholm University. Equipped with an Andor DV438 CCD camera with an E2V 20C CCD chip and Bessel-like *UBVRI* filters.

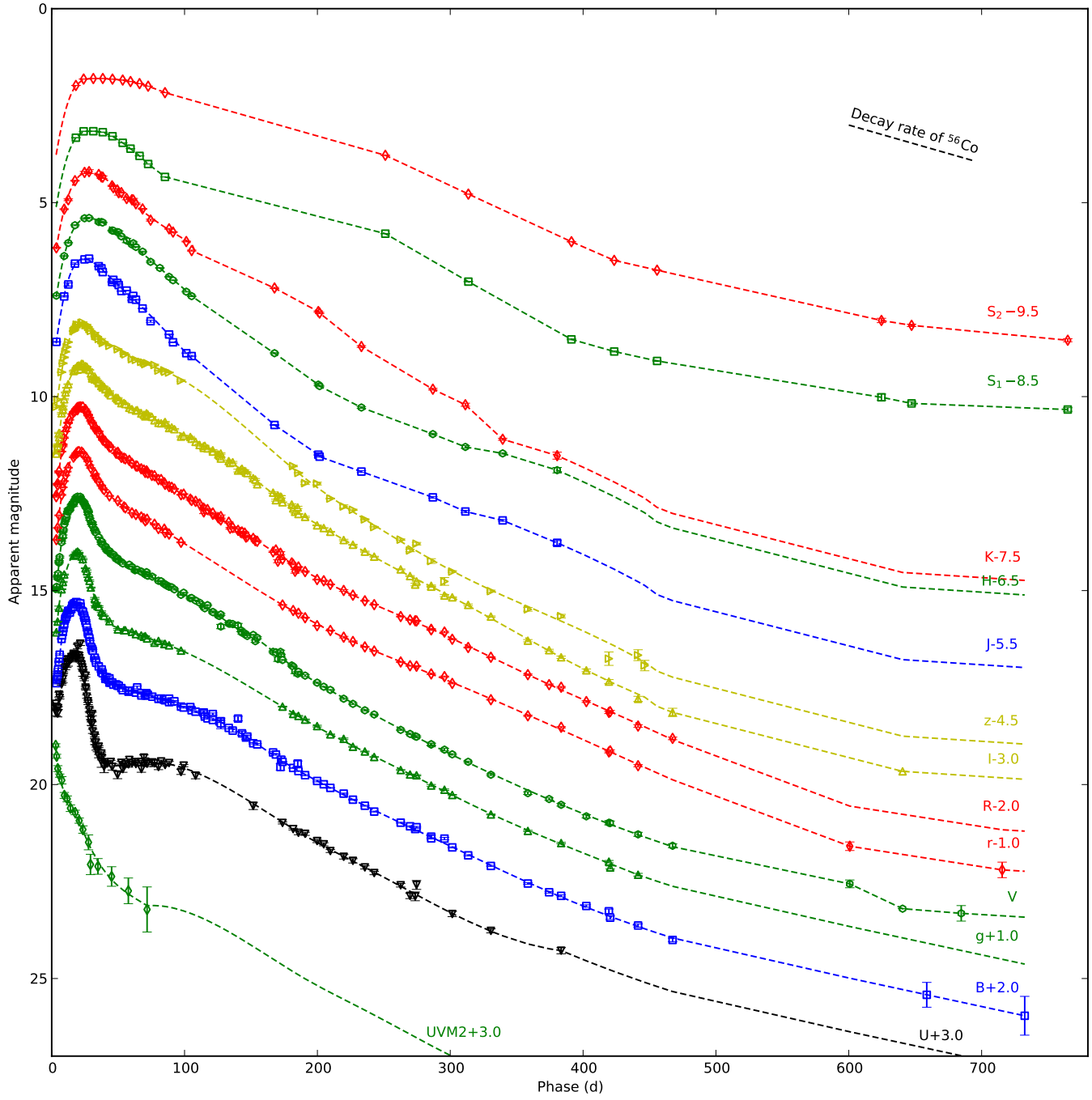

Fig. 1. Apparent UV, optical, NIR and MIR broad-band lightcurves for SN 2011dh. For clarity each band has been shifted in magnitude. Each lightcurve has been annotated with the name of the band and the shift applied. We also show combinations of spline fits, interpolations and extrapolations used in calculations.

2.3. Bolometric evolution

To calculate the bolometric lightcurves we use the spectroscopic and photometric methods described in E14, applied to wavelength regions with and without spectral information, respectively. Combinations of spline fits, interpolations and extrapolations (Sect. 2.1; Figs. 1 and 2) have been used to calculate the magnitudes. Here and throughout the paper, the wavelength regions over which the luminosity is integrated are specified as follows; UV (1900−3300 Å), optical (3300−10000 Å), NIR (10000−24000 Å) and MIR (24000−50000 Å).

Figure 3 shows the <500 days optical-to-NIR pseudo-bolometric lightcurves for SNe 2011dh, 1993J and 2008ax, as calculated with the photometric method, and in Table 1 we tabulate the decline rates at 100, 200 and 300 days. Given the caveat that SNe 1993J and 2008ax are not covered in NIR after ∼250 and ∼150 days, respectively, their optical-to-NIR pseudo-bolometric lightcurves are remarkably similar to the one of SN 2011dh, except for the shift towards higher luminosities mentioned in Sect. 2.2. The decline rates decrease from ∼0.020 mag day^{-1}, roughly twice the decay rate of ^{56}Co, at 100 days to ∼0.015 mag day^{-1} at 300 days. There is however a signifi-

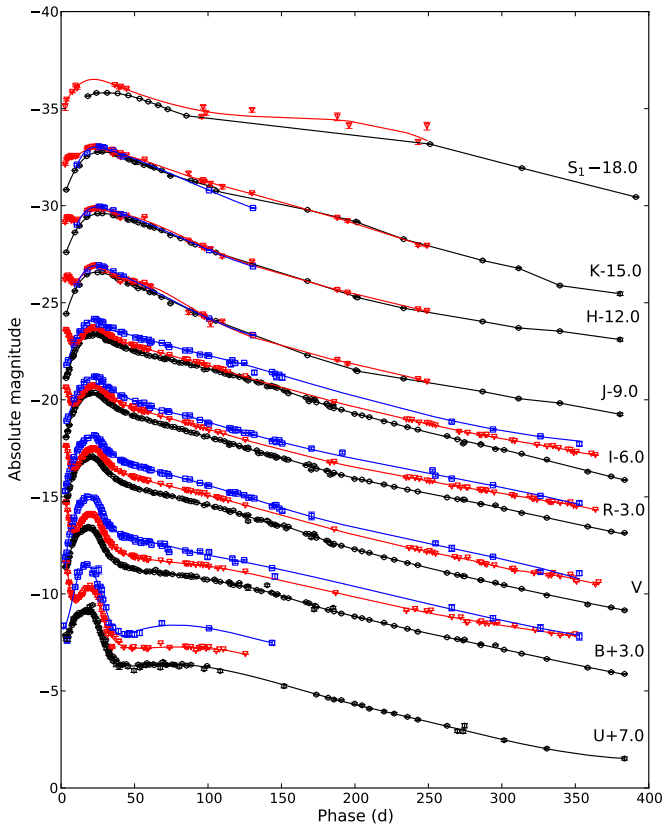

Fig. 2. Absolute optical, NIR and MIR broad-band lightcurves for SNe 2011dh (dots), 1993J (crosses) and 2008ax (pluses).For clarity each band has been shifted in magnitude. Each lightcurve has been annotated with the name of the band and the shift applied. We also show combinations of spline fits, interpolations and extrapolations used in calculations.

cant increase in the decline rate to ∼0.025 mag day^{-1} between 150 and 200 days for SN 2011dh, even more pronounced in the optical pseudo-bolometric lightcurve, not seen for SNe 1993J and 2008ax. For SN 1993J the decline rate becomes increasingly lower towards 300 days as compared to SNe 2011dh and 2008ax, which is consistent with an increasing contribution from circum-stellar medium (CSM) interaction in this phase.

Figure 4 shows the <750 days UV-to-MIR pseudo-bolometric lightcurve for SN 2011dh, as calculated with the combined spectroscopic and photometric methods, and in Table 10 we tabulate the 3−400 days period (for which we have full U to S_2 coverage) for reference. The decline rates are similar to those for the optical-to-NIR pseudo-bolometric lightcurve, but the increase between 150 and 200 days is not as pronounced. Given the caveat that the NIR coverage ends at ∼400 days, the UV-to-MIR pseudo-bolometric lightcurve shows a significant flattening after ∼400 days, and the decline rates for the 467-601 and 601-732 days periods are 0.0088 and 0.0061 mag day^{-1}, respectively. This flattening is also observed in the optical and MIR pseudo-bolometric lightcurves, for which we have full coverage, and after ∼750 days the MIR pseudo-bolometric lightcurve becomes almost flat. The optical decline rates are 0.0095 and 0.0069 mag day^{-1} for the 467−601 and 601−732 days periods, respectively, whereas the MIR decline rates are 0.0069, 0.0031 and 0.0006, for the 456−625, 625−765 and 765−1061 days periods, respectively. The flattening of the late-time lightcurves are discussed in more detail in Sect. 5.

Table 1. Optical and NIR broad-band and optical-to-NIR pseudo-bolometric decline rates at 100, 200 and 300 days for SNe 2011dh, 1993J and 2008ax.

SN	Band	Rate (100 d) (mag day^{-1})	Rate (200 d) (mag day^{-1})	Rate (300 d) (mag day^{-1})
2011dh	*U*	0.011	0.019	0.017
2011dh	*B*	0.014	0.018	0.016
2011dh	*V*	0.019	0.021	0.017
2011dh	*R*	0.021	0.018	0.016
2011dh	*I*	0.019	0.020	0.018
2011dh	*J*	0.036	0.018	0.011
2011dh	*H*	0.029	0.019	0.011
2011dh	*K*	0.020	0.020	0.024
2011dh	*U*-*K*	0.021	0.019	0.016
1993J	*U*	0.006	...	...
1993J	*B*	0.011	0.017	0.012
1993J	*V*	0.019	0.018	0.017
1993J	*R*	0.022	0.014	0.013
1993J	*I*	0.022	0.018	0.013
1993J	*J*	0.041	0.017	...
1993J	*H*	0.033	0.018	...
1993J	*K*	0.022	0.024	...
1993J	*U*-*K*	0.021	0.017	0.013
2008ax	*U*	0.013	...	...
2008ax	*B*	0.015	0.018	0.016
2008ax	*V*	0.022	0.017	0.018
2008ax	*R*	0.023	0.015	0.016
2008ax	*I*	0.018	0.020	0.012
2008ax	*J*	0.035	...	...
2008ax	*H*	0.032	...	...
2008ax	*K*	0.032	...	...
2008ax	*U*-*K*	0.020	0.017	0.015

Figure 5 shows the fractional UV, optical, NIR and MIR luminosities for SN 2011dh. We assume the late-time extrapolated fractions to stay constant and do not use the adjacent colour based extrapolations applied elsewhere. At >100 days the most notable is the strong increase in the MIR fraction between 100 and 250 days, together with a simultaneous decrease in the optical fraction. Also notable is the increase in the NIR fraction between 200 and 400 days caused by the evolution in the J and H bands. The evolution becomes quite uncertain after ∼400 days when the NIR coverage ends, but there seems to be a continuous increase in the MIR fraction, at the expense of the optical fraction. Keeping the uncertainties in mind, it is worth noting the dominance of the optical luminosity even at ∼750 days.

Figure 6 shows the evolution of the SED, overplotted with blackbody fits to the V, I, J, H and K photometry as well as the observed (interpolated) spectra. At >100 days the most notable is again the strong excess (relative to the blackbody fits) developing in the MIR between 100 and 250 days, although an excess in the S_2-band is observed already during the first 100 days (E14). There is also a similar excess (relative to the blackbody fits) developing in the K-band between 100 and 200 days, gradually fading away towards 300 days. The evolution in the K and MIR bands, as well as the behaviour of the pseudo-bolometric lightcurves between 150 and 200 days, are discussed in more

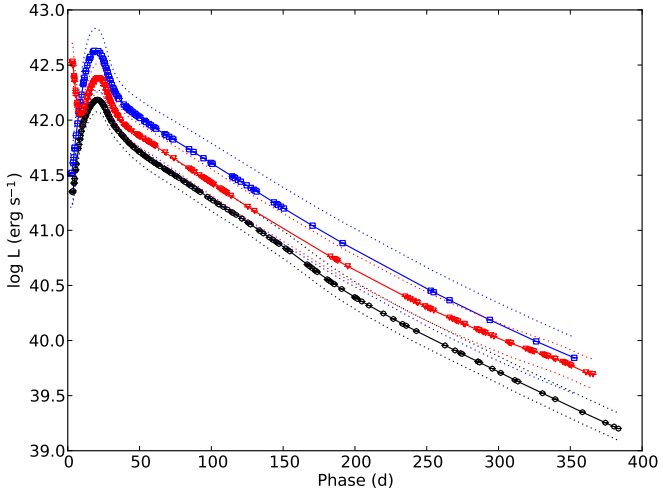

Fig. 3. Optical-to-NIR pseudo-bolometric lightcurve for SNe 2011dh (black circles and solid line), 1993J (red crosses and solid line) and 2008ax (blue pluses and solid line). The upper and lower error bars for the systematic error arising from extinction and distance (dotted lines) are also shown.

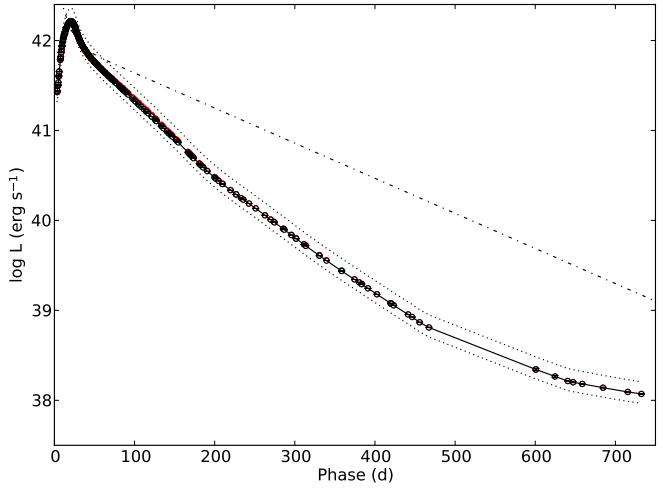

Fig. 4. UV-to-MIR pseudo-bolometric lightcurve for SN 2011dh (black circles and solid line). The upper and lower error bars for the systematic error arising from extinction and distance (black dotted lines) and the radioactive decay chain luminosity of 0.075 $M_\odot$ of ^{56}Ni (black dash-dotted line) are also shown.

detail in Sect. 4.1.5, where we compare the observed lightcurves to results from modelling.

3. Spectroscopy

Here we present observations spanning 100−415 days in the optical and 100−206 days in the NIR, and provide analysis and comparisons with SNe 1993J and 2008ax. Steady-state NLTE modelling of these data, as well as a detailed analysis of the formation of the identified lines and the evolution of their fluxes, are presented in J14. Our analysis is complementary and focus on the line profiles, and what can be learned about the distribution of the material from the nuclear burning zones. Following J14 these are the Fe/Co/He core, the oxygen-rich O/Si/S, O/Ne/Mg and O/C zones, and the helium and hydrogen envelopes. This progression corresponds to the onion-like structure obtained in 1-D modelling (e.g. Woosley & Heger 2007), whereas in multi-D modelling hydrodynamical instabilities results in macroscopic mixing of these zones (e.g. Iwamoto et al. 1997). We adopt a recession velocity of 515 km s^{-1} for SN 2011dh, as estimated from the Hα velocity map in Shetty et al. (2007). For SNe 1993J and 2008ax we adopt the systematic recession velocities for M81 (−34 km s^{-1}; Tully et al. 2008) and NGC 4490 (565 km s^{-1}; Lavaux & Hudson 2011), respectively. The spectroscopic data for SNe 1993J and 2008ax are the same as in E14, except that we also include spectra for SN 2008ax from Milisavljevic et al. (2010), and unpublished spectra for SN 1993J obtained with the WHT and the Isaac Newton Telescope (INT) (P. Meikle et al.; private communication), described in J14.

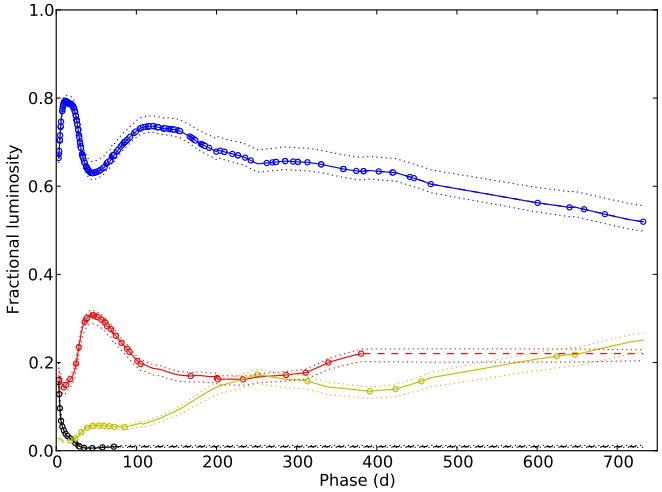

Fig. 5. Fractional UV (black dots), optical (blue dots), NIR (red dots) and MIR (yellow dots) luminosity for SN 2011dh. Interpolations and extrapolations are displayed as solid and dashed lines, respectively. The upper and lower error bars for the systematic error arising from extinction (dotted lines) are also shown.

3.1. Observations

The >100 days data were obtained with the NOT, the TNG, the WHT, the INT, the CA 2.2m, the AS 1.82m and the Gran Telescopio Canarias (GTC). The late-time dataset includes 26 (81 in total) optical spectra obtained at 21 (47 in total) epochs and 2 (20 in total) NIR spectra obtained at 2 (12 in total) epochs. The details of the late-time observations are given in Table 9, and the reductions and calibration procedures are described in E14.

All reduced and calibrated spectra will be made available for download from the Weizmann Interactive Supernova data REPository[2] (WISeREP) (Yaron & Gal-Yam 2012). Figure 7 shows the sequence of observed spectra, where those obtained on the same night using the same instrument have been combined. In addition to this, the 289, 292 and 293 days NOT spectra and the 228, 229, and 231 days INT spectra have been combined to increase the signal to noise ratio (SNR). For clarity some figures in this and the following sections are based on time-interpolations of the spectral sequence (E14), and to further visualize the evolution the spectra have been aligned to a time axis at the right border of the panels. Interpolated spectra are used in the calculations of S-corrections and the bolometric lightcurve (Sect. 2.3). Figure 8 shows the interpolated optical and NIR spectral evolution of SN 2011dh for 5−425 days with a

[2] http://www.weizmann.ac.il/astrophysics/wiserep/

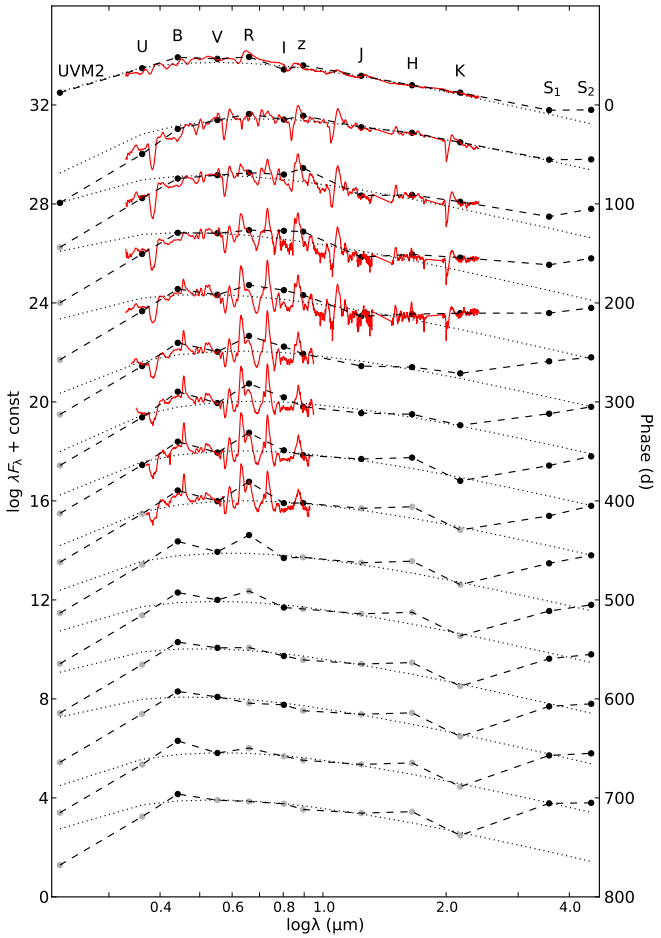

Fig. 6. The evolution of the SED (black dots and dashed lines), overplotted with blackbody fits to the V, I, J, H and K photometry (black dotted lines) as well as the observed (interpolated; Sect. 3.1) spectra (red solid lines). Fluxes based on extrapolated magnitudes are displayed in shaded colour.

20-day sampling. All spectra in this and subsequent figures have been corrected for red-shift and interstellar extinction.

3.2. Line evolution

Figure 9 shows the (interpolated) evolution for all lines identified in J14, and most of these are also marked in Fig. 8. Below we briefly discuss the evolution of the most important lines, and for a detailed discussion we refer to J14. As mentioned, the optical coverage ends at ∼400 days and the NIR coverage at ∼200 days.

There is an emerging emission feature near the rest wavelength of Hα, increasing in strength towards 450 days, but this feature is too narrow (∼5500 km s^{-1} as fitted with the line profile model described in Appendix B.1) to be consistent with the $\gtrsim$11000 km s^{-1} observed for the hydrogen envelope (E14). As discussed in J14 this feature is rather due to [N II] 6548,6583 Å emission originating from the helium envelope. There is also a dip in the [O I] 6300,6364 Å line profile after ∼150 days (Fig. 11), that corresponds well to the early time Hα absorption minimum at ∼11000 km s^{-1} (E14). However, as discussed in Sect. 3.6, this feature repeats in a number of other lines, and is rather due to clumping/asymmetries in the ejecta.

The prominent He I 10830 Å and He I 20581 Å lines show P-Cygni like profiles, extending in absorption to at least ∼10000 km s^{-1}, and are still strong when the NIR coverage ends, whereas the He I 5016 Å line shows a P-Cygni like profile, extending in absorption to ∼5000 km s^{-1}, and fades away at ∼300 days. The He I 5876 Å line is likely scattered away in the Na I 5890,5896 Å line (J14), whereas the He I 6678 Å and He I 7065 Å lines are present at ∼100 days, but then quickly disappear.

The [O I] 6300,6364 Å line appears at ∼100 days, and grows to become the most prominent line at ∼400 days. The O I 7774 Å line shows a P-Cygni like profile until ∼300 days, extending in absorption to ∼8000 km s^{-1}, whereas the [O I] 5577 Å line fades away at ∼300 days. The O I 9263 Å line (blended with the [Co II] 9338,9344 Å line; J14) seems to be present at least until ∼400 days, whereas the O I 11290,11300 Å line is present until the NIR coverage ends. The Mg I] 4571 Å line appears at ∼150 days and increase in strength towards ∼400 days, whereas the Mg I 15040 Å line is present until the NIR coverage ends.

The Na I 5890,5896 line is present with a P-Cygni like profile until the optical coverage ends, extending in absorption to ∼10000 km s^{-1}. The Ca II 3934,3968 Å line shows a strong absorption profile, extending to ∼15000 km s^{-1}, and as the Ca II 8498,8542,8662 Å line (blended with the [C I] 8727 Å line; J14) it is present until the optical coverage ends. The latter shows an absorption component at ∼100 days, which quickly disappears, and the Ca II 8498,8542 Å contribution fades away towards ∼400 days. The [Ca II] 7291,7323 Å line appears at ∼100 days, soon becomes the most prominent line, and has a growing red wing extending to ∼10000 km s^{-1}, which could be caused by [Ni II] 7378,7411 Å emission (J14).

The [Fe II] 7155 Å line appears at ∼200 days in the blue wing of the [Ca II] 7291,7323 Å line and is present until the optical coverage ends. A distinct feature near 16450 Å, that could be either [Fe II] 16440 Å or [Si I] 16450 Å is present until the NIR coverage ends. The [Co II] 9338,9344 Å line (blended with the O I 9263 Å line; J14) seems to be present at least until ∼300 days, whereas the [Co II] 10190,10248,10283 Å and [Co II] 15475 Å lines are present until the NIR coverage ends.

3.3. CO emission

The upper left panel of Fig. 10 shows the observed K-band spectrum at 206 days compared with the preferred steady-state NLTE model spectrum at 200 days, flux calibrated with the observed K-band flux at 206 days. The model (12F; see Sect. 4.1.2 and Appendix C.4) includes dust but not CO emission. The CO first overtone (Δv=2) emits between 2.25 and 2.45 μm and we have marked the location of the band heads, which are not sharp due to the Doppler broadening of the individual transitions contributing. There is a strong excess in this region as compared to the model spectrum, the integrated flux being 1.0×10^{-14} erg s^{-1} cm^{-2}. The contribution from this flux to the K-band flux is negligible though, due to the weak overlap with this band. We have used a simple LTE CO model described in Spyromilio et al. (1988) to provide a fit to the emission. The ratio of the band head emission is a diagnostic of the temperature of the CO, and the shape of the band heads a diagnostic of the expansion velocity of the CO gas. In the upper right panel of Fig. 10 we show the combined CO model and preferred steady-state NLTE model spectrum. The shape of the observed emission and the agreement with the simple CO model provides strong support for the identification of this feature with emission from the first overtone of CO. The temperature in the CO model is 2300 K and

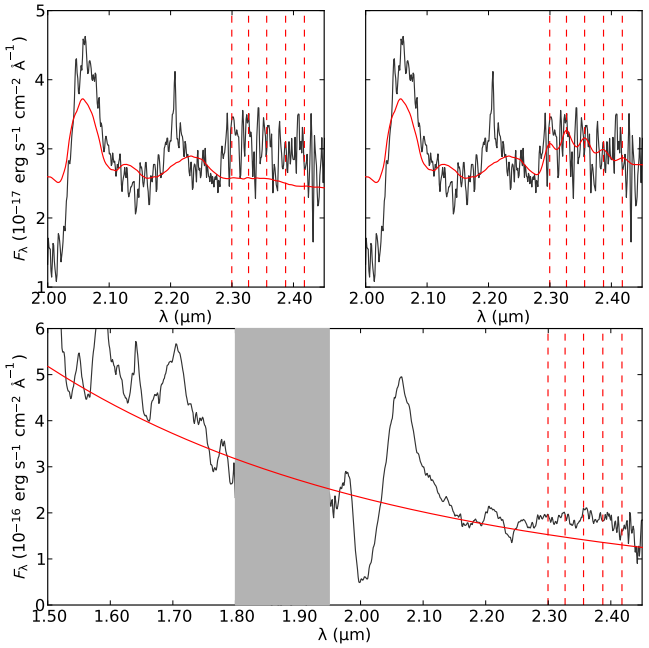

Fig. 10. Upper left panel: Observed (black solid line) and preferred steady-state NLTE model (red solid line) *K*-band spectra at 206 and 200 days, respectively. Upper right panel: The same, but with CO LTE model emission added to the steady-state NLTE model spectra. The CO overtone band heads have been marked by red dashed lines and the steady-state NLTE model spectra flux calibrated with the observed *K*-band flux at 206 days. Lower panel: Observed (black solid line) *H* and *K*-band spectrum at 89 days as compared to a blackbody fit to the continuum (red solid line).

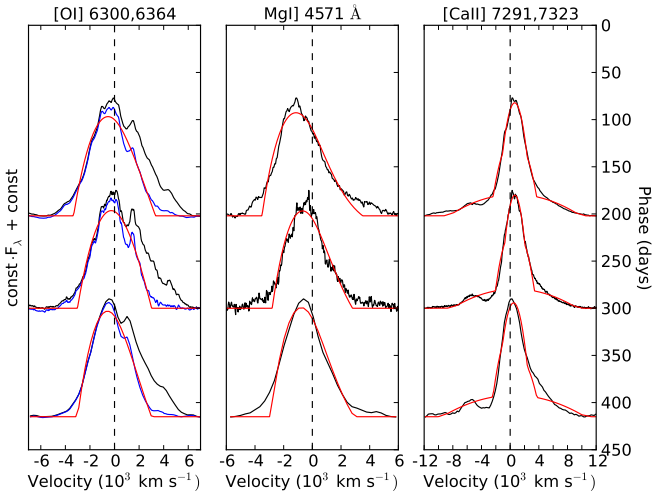

Fig. 11. The [O I] 6300,6364 Å (left panel; black), decomposed [O I] 6300 Å (left panel; blue), Mg I] 4571 Å (middle panel) and [Ca II] 7291,7323 Å (right panel) lines at selected epochs, as compared to line profile fits (red). The [O I] 6300 Å line was decomposed with the method described in Appendix B.1.

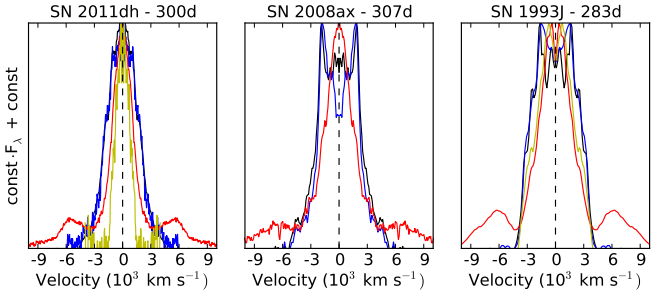

Fig. 12. Continuum subtracted mirrored blue-side profiles for the [O I] 6300,6364 Å (black), Mg I] 4571 Å (blue), [Ca II] 7291,7323 Å (red) and [Fe I] 7155 Å (yellow) lines for SNe 2011dh, 2008ax and 1993J at 300, 307 and 283 days respectively. The [Fe I] 7155 Å line is only shown for SN 2011dh.

the emission region extends to 1500 km s^{-1}. The lower panel of Fig. 10 shows the observed *H* and *K*-band spectrum at 89 days. As this spectrum was obtained before 100 days, where the steady-state condition needed for the NLTE modelling is not satisfied, we instead use a blackbody fit to estimate the continuum. Although not as convincing as at 206 days, there is a clear excess in the region where we expect CO first-overtone emission, the integrated flux being 7.2×10^{-14} erg s^{-1} cm^{-2}. The contribution from this flux to the *K*-band flux is again negligible. In the absence of a model for the underlying emission we have not tried to fit the excess emission with the LTE CO model, but the structure of the feature shows a reasonable agreement with the expected positions of the band heads.

3.4. Line emitting regions

The sizes of the line emitting regions are related to the distribution of the material from the different nuclear burning zones, determined by hydrodynamical instabilities in the explosion. In J14 we find the Mg I lines to arise from the O/Ne/Mg zone, the O I lines to arise from the O/Ne/Mg zone and, depending on the amount of molecular (CO and SiO) cooling, the O/C and O/Si/S zones. We also find the [Ca II] 7291,7323 Å line to arise mainly from the Si/S zone and the Fe II and Co II lines to arise from the Fe/Co/He zone. To measure the sizes of the line emitting regions, we fit a simple model for optically thin line emission to the observed line profiles. The model has a constant emissivity, includes an absorptive continuum opacity to mimic blue-shifts caused by obscuration, and the details are given in Appendix B.1. The fits have been applied to lines for which the scattering contribution appears to be small (no absorption component observed), the SNR is good and contamination from other lines is likely to be small. The results are given in Table 2 and a selection of fits shown in Fig. 11. The estimated radii of the O I and Mg I line emitting regions of 2900−3400 and 2700−3600 km s^{-1}, respectively, are similar, whereas the estimated radii of the [Ca II] 7291,7323 Å and the Fe II and Co II line emitting regions of 2100−2500 and 1600−1800 km s^{-1}, respectively, are progressively smaller. This progression is consistent with the (unmixed) onion-like structure of the nuclear burning zones, and suggests incomplete mixing of the oxygen, Si/S and Fe/Co/He material. This is in agreement with results from multi-D hydrodynamical modelling, e.g. the 2-D hydrodynamical modelling of SN 1993J by Iwamoto et al. (1997), which shows significant differences in the distribution of the oxygen and Fe/Co/He material.

We have also compared the radii of the line emitting regions to those of SNe 1993J and 2008ax. For SN 1993J the estimated radii are 4000−4100 and 3700−3900 km s^{-1} for the [O I] 6300 Å and Mg I] 4571 Å lines, respectively, and 3000−3400 km s^{-1} for the [Ca II] 7291,7323 Å line. For SN 2008ax the estimated radii are 3900−4000 and 3400−3600 km s^{-1} for the [O I] 6300 Å and Mg I] 4571 Å lines, respectively, and 2600−3000 km s^{-1}

Table 2. Radii of the line emitting regions as measured from line profile fits. The [O I] 6300 Å line was decomposed with the method described in Appendix B.1. The fitted [Ca II] 7293/7323 Å and [Co II] 10190/10248, 10190/10283 Å line ratios are given in parenthesis.

Phase (d)	[O I] 6300 Å (km s^{-1})	Mg I] 4571 Å (km s^{-1})	Mg I 15040 Å (km s^{-1})	[Ca II] 7293,7323 Å (km s^{-1})	[Fe II] 7155 Å (km s^{-1})	[Co II] 10190,10248,10283 Å (km s^{-1})
89	...	...	3500	...	...	1800 (0.44,0.02)
202	3400	3600	...	2400 (1.09)	...	...
206	...	...	3200	...	...	1800 (0.56,0.39)
300	3100	2800	...	2100 (1.05)	1600	...
415	2900	2700	...	2500 (0.39)	1700	...

for the [Ca II] 7291,7323 Å line. These radii are larger than for SN 2011dh, and larger for SN 1993J than for SN 2008ax. The radii of the Mg I] 4571 Å and the [O I] 6300 Å line emitting regions are again similar, and the radius of the [Ca II] 7291,7323 Å line emitting region is again smaller, suggesting incomplete mixing of the oxygen and Si/S material also for SNe 1993J and 2008ax. Figure 12 shows mirrored blue-side line profiles for the [O I] 6300 Å, Mg I] 4571 Å, [Ca II] 7291 Å and [Fe I] 7155 Å lines for SNe 1993J, 2008ax and 2011dh at ~300 days. The blue side is less affected by obscuration, and contamination from the [O I] 6364 Å and [Ca II] 7323 Å lines to the [O I] 6300 Å and [Ca II] 7291 Å lines is probably modest. This figure nicely illustrates the different sizes of the line emitting regions discussed, and also shows a remarkable similarity of the blue-side [O I] 6300 Å and Mg I] 4571 Å line profiles for all SNe. For SN 2011dh this similarity persists also in small scale fluctuations (Sect. 3.6), which suggests these lines to arise mainly from the O/Ne/Mg zone, and the contributions from the O/C and O/Si/S zones to the [O I] 6300 Å flux to be modest.

3.5. Line asymmetries

Line asymmetries may be caused by intrinsic asymmetries in the ejecta, radiative transfer effects, or blends with other lines. To measure these we calculate the first wavelength moment of the flux (center of flux; Appendix B.2). The upper panel of Fig. 13 shows the center of flux velocities for a selection of lines between 108 and 415 days for SN 2011dh. At early times the [O I] 6300,6364 Å, [O I] 5577 Å and Mg I] 4571 Å lines all show significant blue-shifts, which gradually disappear towards 400 days. As shown in the lower panel of Fig. 13, such blue-shifts are also present, and even more pronounced for SNe 1993J and 2008ax, but in this case the blue-shifts saturate at ~500 km s^{-1} after 200 days. In J14 we provide a thorough discussion of these blue-shifts, and suggest the cause to be obscuration of receding-side emission by line-blocking in the core. We find no significant blue-shifts in the O I 11300 Å, O I 13164 Å and Mg I 15040 Å lines for SNe 2011dh and 2008ax in support of this hypothesis, as line-blocking is less effective in the NIR (J14). After ~250 days we instead see increasing red-shifts in the [Ca II] 7291,7323 Å and Ca II 8498,8542,8662 Å lines for SN 2011dh, likely produced by blends with the [Ni II] 7378,7411 Å and [C I] 8727 Å lines, respectively (J14). Given our interpretation of the line-shifts, the systematic redward trend seen in most lines between 250 and 400 days for SN 2011dh is coincidental.

Obscuration of receding-side emission may also be produced by dust in the ejecta, and as our steady-state NLTE models have a homogeneous dust opacity in the core (Sect. 4.1), in order to explain the behaviour of the lightcurves for SN 2011dh between 100 and 250 days (Sects. 2.3), it is not entirely clear how to disentangle the effects of line-blocking and dust. The version of the preferred model used in this work (12F) has an optical depth of 0.44, which is found to best reproduce the observed lightcurves, whereas the original version presented in J14 (12C) has an optical depth of 0.25. This lower value gives a worse reproduction of the lightcurves, but produce smaller blue-shifts, which seems to be in better agreement with observations. Using our line profile model and assuming a size of the line-emitting region of 3000 km s^{-1} (Sect. 3.4), we find blue-shifts of the center of flux of 150 and 250 km s^{-1} for optical depths of 0.25 and 0.44, respectively. At 415 days, when the effect from line-blocking would be the least, the center of flux for the [O I] 6300,6364 Å and Mg I] 4571 Å lines, which arise solely from the core (J14), shows a red-shift of ~100 km s^{-1} and a blue-shift of ~100 km s^{-1}, respectively. The absence of significant blue-shifts in these lines at 415 days suggests a small optical depth of the dust and indicate that, if the optical depth is as high as 0.44, the dust can not be homogeneously distributed within the core. It also suggests that the relatively large blue-shifts seen in these lines at earlier epochs can be attributed to the line-blocking effect.

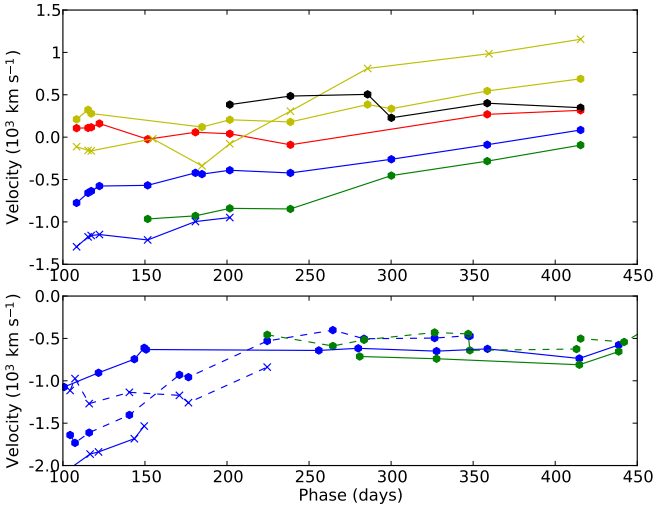

Fig. 13. Upper panel: Center of flux velocities for the [O I] 6300,6364 Å (blue circles), [O I] 5577 Å (blue pluses), Mg I] 4571 Å (green circles)), [Ca II] 7291,7323 Å (yellow circles), Ca II 8498,8542,8662 Å (yellow crosses), Na I 5890,5896 Å (red circles) and [Fe II] 7155 Å (black circles) lines for SN 2011dh. Lower panel: Center of flux velocities for the [O I] 6300,6364 Å (blue circles), [O I] 5577 Å (blue pluses) and Mg I] 4571 Å (green circles) lines for SNe 1993J (dashed lines) and 2008ax (solid lines).

3.6. Small scale fluctuations

Small scale fluctuations in the line profiles may provide evidence for a clumpy ejecta, as previously demonstrated for SNe 1987A (Stathakis et al. 1991; Chugai 1994) and 1993J (Spyromilio 1994; Matheson et al. 2000). In a simplified way we may represent the material of some nuclear burning zone by a number of randomly distributed clumps, having a typical size and occupying some fraction of the ejecta volume (filling factor). The small scale fluctuations then arise from statistical fluctuations in the distribution of the clumps, the RMS (Root Mean Square) of the fluctuations increasing with decreasing number of clumps or filling factor, or increasing size of the clumps.

Figure 14 shows small scale fluctuations in the [O I] 6300,6364 Å, [O I] 5577 Å, O I 7774 Å, Mg I] 4571 Å and Na I 5890,5896 Å lines at 202 and 300 days. The resolution is ~600 and ~250 km s^{-1} in the 202 and 300 days spectra, respectively, and the large scale (>1000 km s^{-1}) structure has been subtracted with the method described in Appendix B.4. In the upper left panel we show a comparison of the [O I] 6300 Å line at 202 and 300 days, and there is not much evolution in the small scale structure during this period. We identify 8 features marked A-H with a FWHM between 300 and 600 km s^{-1} present at both epochs. The G and H features interpreted as belonging to the [O I] 6364 Å line, match very well with the E and F features interpreted as belonging to the [O I] 6300 Å line, so these are likely to be repetitions. Subtracting the [O I] 6364 Å flux using the method described in Appendix B.1, and minimizing the RMS of the small scale fluctuations redwards 3000 km s^{-1}, we find a line ratio of 2.9 at 202 and 300 days to give a complete removal of features G and H. This ratio is close to the 3.1 expected for optically thin emission and consistent with the results in J14.

In the upper right panel we show the decomposed [O I] 6300 Å line at 202 and 300 days, and in the lower left panel we show a comparison to the Mg I] 4571 Å line at 300 days. All features except B are clearly identified in both lines and the agreement is good. The features on the red side are weaker for the Mg I] 4571 Å line, which is consistent with the larger red-side flux deficit for this line (Fig. 11), but the relative (normalized with the large scale flux) strength of all features are similar. The good agreement suggests that the [O I] 6300 Å and Mg I] 4571 Å lines arise from the same nuclear burning zones. This, in turn, suggests that these lines arise mainly from the O/Ne/Mg zone, and that the contributions from the O/Si/S and O/C zones to the [O I] 6300 Å flux are modest (J14, Sect. 3.4).

In the lower right panel we show a comparison of the decomposed [O I] 6300 Å line and the [O I] 5577 Å, O I 7774 Å and Na I 5890,5896 Å lines at 202 days. The E and F features are clearly identified in all of these lines, whereas the other features are only seen in the [O I] 6300 Å line , but since these are weaker it is possible that they are just too faint to be seen in the other lines. The small scale fluctuations in the [Ca II] 7291,7323 Å line (not shown) do not match very well with those in the [O I] 6300 Å line, and the relative strength of the features is weaker. These results are consistent with the results in J14, where the oxygen lines are found to arise from the oxygen-rich zones and the Na I 5890,5896 Å line partly from the O/Ne/Mg zone, whereas the [Ca II] 7291,7323 Å line is found to arise mainly from Si/S zone.

Shivvers et al. (2013) presented an analysis of the [O I] 6300,6364 Å, O I 7774 Å and Mg I] 4571 Å lines at 268 days, where they by Gaussian decomposition find two narrow features, likely corresponding to our E and F features, repeating

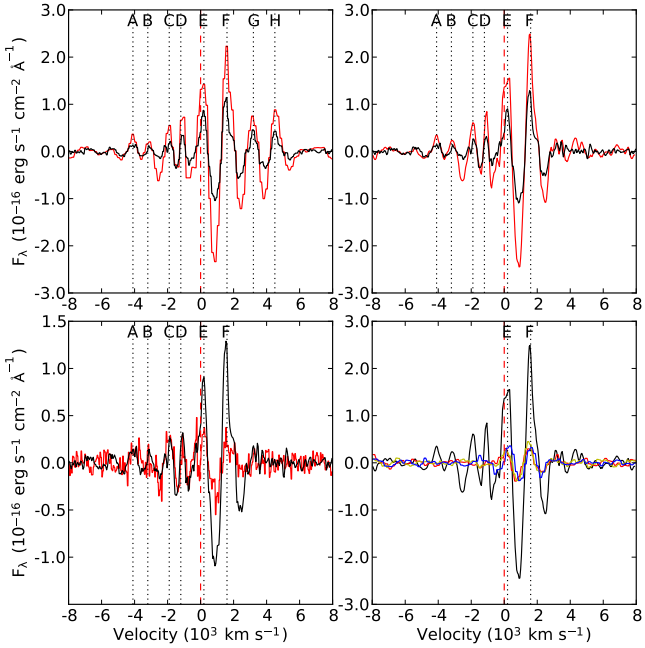

Fig. 14. Comparison of large scale subtracted line profiles. The upper left panel shows the [O I] 6300,6364 Å line at 202 (red) and 300 (black) days. The upper right panel shows the decomposed [O I] 6300 Å line at 202 (red) and 300 (black) days. The lower left panel shows the decomposed [O I] 6300 Å line (black) and the Mg I] 4571 Å line (red) at 300 days. The lower right panel shows the decomposed [O I] 6300 Å line (black) and the [O I] 5577 Å (red), O I 7774 Å (green) and Na I 5890,5896 Å (blue) lines at 202 days.

in all these lines, in agreement with our analysis. Matheson et al. (2000) presented an analysis of small scale fluctuations in the spectra of SN 1993J, and found a good agreement between the fluctuations in the [O I] 6300 Å, [O I] 5577 Å and O I 7774 Å lines, in agreement with our results for SN 2011dh. Surprisingly, they did not find a good agreement between the fluctuations in the [O I] 6300 Å and Mg I] 4571 Å lines. One possible explanation is that the [O I] 6300 Å line is dominated by flux from the O/Ne/Mg zone for SN 2011dh, but not for SN 1993J (see above). Filippenko & Sargent (1989) presented an analysis of small scale fluctuations in the spectra of the Type Ib SN 1985F. Similar to our analysis they found repetitions of the identified features in the [O I] 6300 Å and 6364 Å lines, and a line ratio close to 3 using the strongest feature.

Matheson et al. (2000) applied the statistical model by Chugai (1994) to their spectra of SN 1993J, giving a filling factor of ~0.06 for oxygen zone material, distributed within a sphere with 3800 km s^{-1} radius. Using their estimated typical clump size of 300 km s^{-1}, this corresponds to ~900 clumps. The model requires the radius of the sphere containing the clumps, the typical size of the clumps and the RMS of relative flux fluctuations in lines originating from the clumps. In the case of SN 2011dh, we adopt a radius of the sphere containing the bulk of the oxygen zone material of ~3500 km s^{-1}, based on the estimates of the O I and Mg I line emitting regions in Sect. 3.2. For SN 1987A a typical clump size of 120 km s^{-1} was estimated from the power spectrum of the [O I] 6300 Å line by Stathakis et al. (1991), using high-resolution spectroscopy, but it is not clear how this was done by Matheson et al. (2000). As we do not have high-resolution spectroscopy for SN 2011dh, we can only estimate an

upper limit on the typical clump size, taken to be 300 km s^{-1}, the smallest size of the features seen. The RMS of the relative flux fluctuations in the inner part (±2000 km s^{-1}, see Chugai 1994) of the sphere is ∼0.13 and ∼0.09 at 300 days for the decomposed [O I] 6300 Å line and the Mg I] 4571 Å line, respectively. Taking the latter value as a lower limit and applying Chugai (1994, eq. 11), we find an upper limit on the filling factor of oxygen zone material (within the sphere) of ∼0.07, and a lower limit on the number of oxygen zone clumps of ∼900. These values are similar to the values estimated by Matheson et al. (2000) for the clumping of oxygen zone material in SN 1993J.

4. Lightcurve modelling

Modelling of nebular-phase pseudo-bolometric or broad-band lightcurves is rare, and it is therefore of interest to examine this case using the high quality observations obtained for SN 2011dh. To accomplish this we use the nebular-phase spectral synthesis code described in Jerkstrand et al. (2011, 2012), hereafter referred to as the steady-state NLTE code. In J14 we present spectra for a set of models, and here we present pseudo-bolometric and broad-band lightcurves for the same models. As this code assumes steady-state, the models are limited to $\gtrsim$100 days, and due to the complexity of the physics, a restricted volume of parameter space is covered. Consistent modelling of the diffusion-phase *and* nebular-phase lightcurves is desirable, and to facilitate this we make use of HYDE, a hydrodynamical code described in Ergon et al. (2015, hereafter E15) and summarized in Appendix D. HYDE is capable of evolving the SN from the explosion into the nebular phase, but is limited to bolometric lightcurve modelling, so in practice it can only be used at $\lesssim$100 days when the bolometric correction (BC) is small. Due to its simplicity it is fast, and in E15 we construct a grid of SN models covering a large volume of parameter space. Feeding all these models into the steady-state NLTE code is not feasible, but by combining the advantages of each code we are able to stretch the limitations. First, to extend the coverage of the J14 models to early times, we calculate <100 days bolometric lightcurves for these with HYDE. Secondly, to extend the coverage of the E15 model grid to late times, we determine the BC with the steady-state NLTE code, and use it to fit the <400 days optical-to-MIR pseudo-bolometric lightcurve to the model grid.

4.1. Steady-state NLTE modelling of the 100−500 days pseudo-bolometric and broad-band lightcurves.

In J14 we present a set of spectral models for Type IIb SNe, with the specific aim to model SNe 1993J, 2008ax and, in particular, SN 2011dh. Here we present synthetic 100−500 days pseudo-bolometric and broad-band lightcurves for these models, constructed using the standard system filter response functions specified in E14. The preferred model for SN 2011dh, presented in J14, and refined in this paper with respect to dust, has been chosen to give the best agreement with both nebular spectra and the pseudo-bolometric and broad-band lightcurves. In J14 we discuss the constraints on the model parameters provided by the nebular spectra, and here we discuss the constraints provided by the lightcurves. In this work we restrict the set of models (J14, table 3) to the model families differing in a single parameter (J14, table 4), and two additional models (12E and 12F) described in Appendix C.4. These models differ from model 12C only in the absence (12E) and the properties (12F) of the dust.

4.1.1. Model parameters

The models vary in the following parameters: initial mass (12, 13 or 17 M$_\odot$), macroscopic mixing (medium or strong), density contrast (low or high), positron trapping (local or non-local), molecular cooling (complete or none) and dust ($\tau_{\rm dust}$=0, 0.25 or 0.44). The former four parameters are described in detail in J14. In short, the initial mass parameter determines the overall properties of the ejecta model (e.g. mass and abundances), whereas the macroscopic mixing and contrast factor parameters mimic the mixing of the nuclear burning zones and subsequent expansion of the Fe/Co/He clumps arising in mutli-D modelling. The positron trapping parameter mimics the effect of a magnetic field (on the positron trapping). Note that the strong mixing models differ from the medium mixing models only in that 50 percent of the Fe/Co/He material is mixed into the helium envelope, and that the mass of the ^{56}Ni is fixed at 0.075 M$_\odot$ (see Sect. 4.2).

The modelling does not include a treatment of the formation of molecules and dust in the ejecta, but the effects of these are included in a simplified way as described in Appendices C.3 and C.4. The treatment of molecules only supports two extremes, no emission or complete dominance of the cooling in the O/C and O/Si/S zones by CO and SiO emission. This is motivated by the fact that molecules are efficient coolers and tend to dominate the cooling once formed. Dust absorption is represented as a grey absorptive opacity in the core, and the emission as blackbody emission. Absorption is turned on at 200 days, and the optical depth chosen to reproduce the optical pseudo-bolometric lightcurve, whereas the temperature of the blackbody emission is determined from fits to the K and S_1 bands.

4.1.2. The preferred model.

The preferred model presented in J14 (12C) has an initial mass of 12 M$_\odot$, strong macroscopic mixing, local positron trapping, no molecular cooling, dust with $\tau_{\rm dust}$=0.25 and a high density contrast. However, in this work we use a refined version of the preferred model (12F), which differs only in the optical depth ($\tau_{\rm dust}$=0.44) and the temperature of the dust (Appendix C.4). The prefix "preferred" is used to distinguish from a best-fit model, as the one discussed in Sect. 4.2. It should be noted that the good spectroscopic agreement found for model 12C in J14 does not necessarily apply to model 12F, but the differences are likely to be small (Appendix C.4). Figures 15 and 16 show the 100−500 days preferred model and observed pseudo-bolometric lightcurves. In these figures, and in a number of figures that follows, we have normalized the luminosity with the decay chain luminosity of the mass of ^{56}Ni, which (to first order) removes the dependence on this quantity. The preferred model shows a good agreement with observations, the differences being $\lesssim$10 and $\lesssim$15 percent for the optical and optical-to-MIR pseudo-bolometric lightcurves, respectively. However, after ∼400 days the observed optical pseudo-bolometric lightcurve flattens and starts to diverge from that of the preferred model. This flattening continues after 500 days and is discussed in Sect. 5. Figure 17 shows the preferred model and observed broad-band lightcurves. The preferred model shows an overall good agreement with observations, the differences being mostly $\lesssim$0.3 mag, but there are some notable exceptions, as the U and S_2 bands. The discrepancy seen in the optical pseudo-bolometric lightcurve after ∼400 days is also reflected in the B, g and V bands. The discrepancy in the S_2-band is discussed further in Sect. 4.1.5.

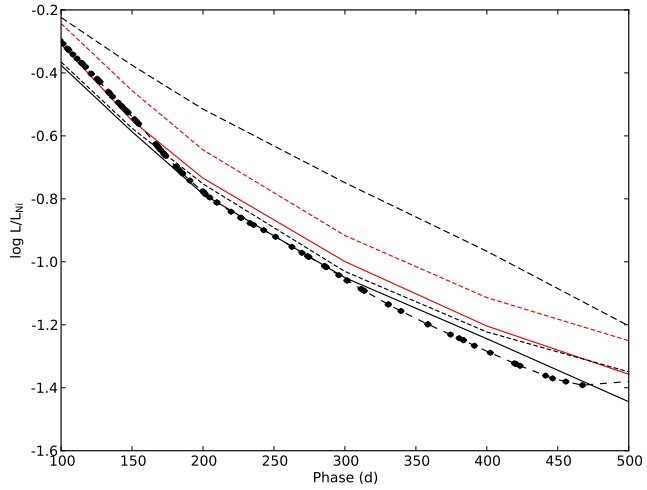

Fig. 15. The 100−500 days observed (black circles) and J14 model optical-to-MIR pseudo-bolometric lightcurves normalized to the radioactive decay chain luminosity of 0.075 $M_\odot$ of ^{56}Ni. Selected representatives (12A,12F,13A,13C,17A) of the model families differing in initial mass and macroscopic mixing are shown and displayed as follows: 12 $M_\odot$ (solid lines), 13 $M_\odot$ (short dashed lines), 17 $M_\odot$ (long dashed lines), medium mixing (red), strong mixing (black). In this colour coding the preferred model is displayed as a black solid line.

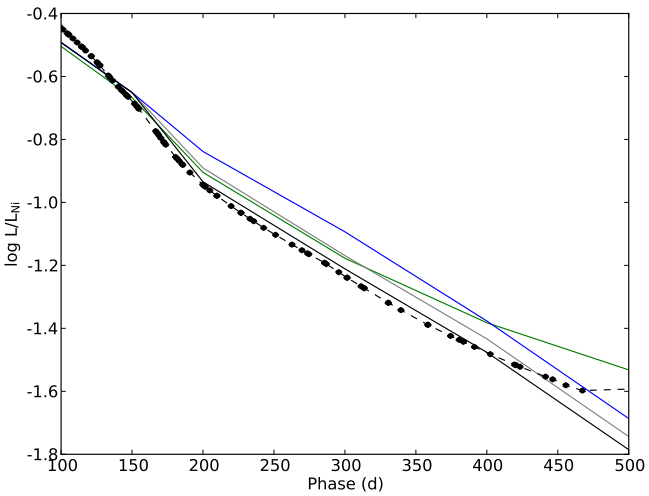

Fig. 16. The 100−500 days observed (black circles) and J14 model optical pseudo-bolometric lightcurves normalized to the radioactive decay chain luminosity of 0.075 $M_\odot$ of ^{56}Ni. The preferred model (12F; black solid line), model 12C (grey solid line) and model 12E (blue solid line), which differ only in the optical depth (12F; 0.44, 12C; 0.25, 12E; 0) and temperature of the dust, are shown together with model 12B (green solid line), which differs from model 12C only in the positron trapping (12C; local, 12B; non-local).

4.1.3. Calculation of the <100 days bolometric lightcurves with HYDE

Only after ∼100 days, steady-state is satisfied and the NLTE code can be used. To investigate the behaviour of the models in the early phase, we use HYDE in homologous mode to produce 3−100 days bolometric lightcurves. The J14 models are first (homologously) rescaled to day one, and then evolved with HYDE through the 1−100 days evolution. The initial temperature profile at 1 day is adopted from the best-fit hydrodynamical model for SN 2011dh (Sect. 4.2), with the mixing of the ^{56}Ni

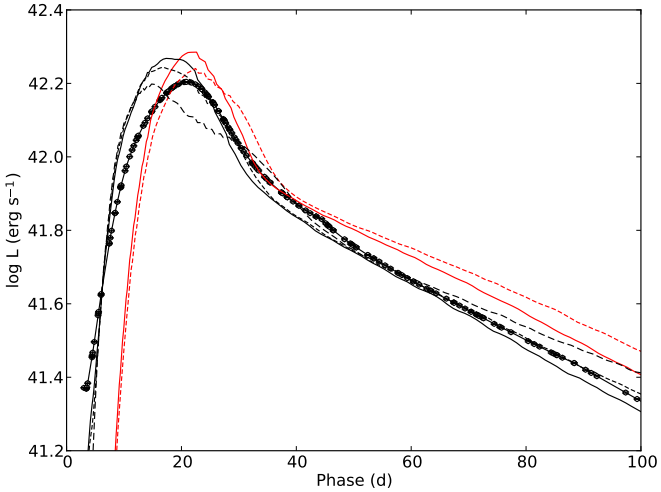

Fig. 18. The 3−100 days J14 model bolometric lightcurves calculated with HYDE, as compared to the observed optical-to-MIR pseudo-bolometric lightcurve (black circles). The model families differing in initial mass and macroscopic mixing are shown and displayed as follows: 12 $M_\odot$ (solid lines), 13 $M_\odot$ (short dashed lines), 17 $M_\odot$ (long dashed lines), medium mixing (red), strong mixing (black). In this colour coding the preferred model is displayed as a black solid line.

adjusted to match that of the J14 models. The subsequent evolution is not sensitive to the choice of initial temperature profile, as it is powered by the continuous injection of radioactive decay energy. Figure 18 shows the 3−100 days bolometric lightcurves for the J14 model families differing in initial mass and macroscopic mixing, as compared to the observed optical-to-MIR pseudo-bolometric lightcurve. The other J14 model parameters have negligible influence on the bolometric lightcurve (Appendix C.1), and the optical-to-MIR BC is likely >−0.15 mag during this period (Appendix C.2), so the comparison is justified. The preferred model shows an overall agreement with observations, although the peak occurs a few days earlier and is overproduced by ∼0.2 mag.

4.1.4. Constraints on the model parameters

Here we discuss the constraints obtained from the lightcurves on the model parameters, except for the molecular cooling and dust parameters, which are discussed separately in Sect. 4.1.5. As explained in Appendix C.1, a factorisation of the model lightcurves into bolometric lightcurves and BCs is useful for the analysis, as the bolometric lightcurve depends significantly only on the initial mass and macroscopic mixing, whereas the other parameters only significantly affect the BCs. However, these quantities can not be compared with observations, and observational counterparts are the (optical-to-MIR) pseudo-bolometric lightcurve and the pseudo-BCs. The pseudo-BC for band X is abbreviated $BC_{X,P}$, and differs from BC_X only in that it is based on the (optical-to-MIR) pseudo-bolometric luminosity. Figures 18 and 15 show the 3−100 days and 100−500 days observed optical-to-MIR pseudo-bolometric lightcurves, respectively, as compared to the model families differing in initial mass and macroscopic mixing[3]. Fig. 19 shows the observed and model pseudo-BCs, where we have selected the bands and parameter model families from which useful constraints can be obtained. Additional constraints can be obtained from the broad-

[3] The 3−100 days model lightcurves are bolometric (Sect. 4.1.3)

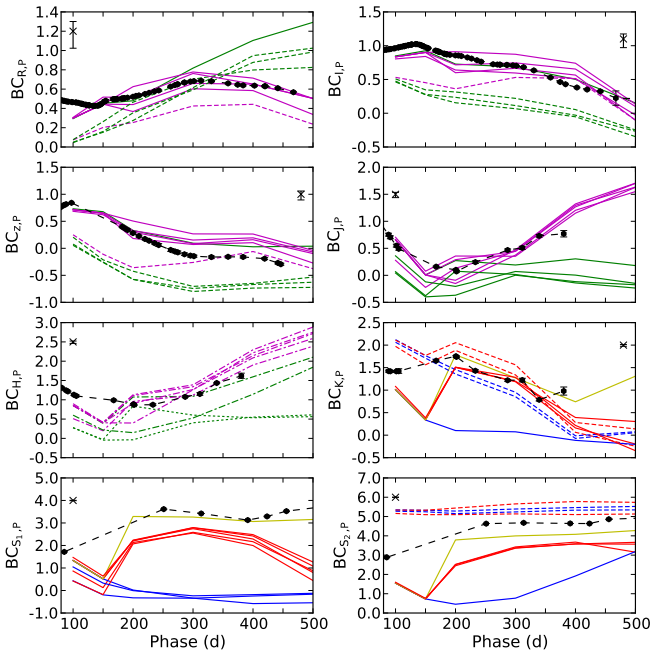

Fig. 19. The 100−500 days observed (black circles) and J14 model pseudo-BCs for selected bands and selected parameter families. The model parameter families are displayed as follows: complete molecular cooling (dashed lines), no molecular cooling (solid lines), high density contrast (dotted lines), low density contrast (dashed-dotted lines), local positron trapping (magenta), non-local positron trapping (green), $\tau_{\rm dust}$=0 (blue), $\tau_{\rm dust}$=0.25 (red), $\tau_{\rm dust}$=0.44 (yellow). 17 $M_\odot$ and medium mixing models are not displayed. To help reading the figures we display fitted magnitudes (Sect. 2.1) for well sampled bands. The error bars arising from the extinction is marked in the upper left or right corner.

band lightcurves (Fig. 17; all models) and the optical pseudo-bolometric lightcurves (Fig. 16; selected models differing in the positron trapping and the properties of the dust).

Initial mass and macroscopic mixing Affect both the bolometric lightcurve and the BCs. The constraints from the optical-to-MIR pseudo-bolometric lightcurve are likely better obtained with the procedure used in Sect. 4.2, but in agreement with those results, 17 $M_\odot$ and medium mixing models seem to be excluded. In particular the tail luminosity becomes to high for 17 $M_\odot$ models and the rise to peak luminosity begins too late for medium mixing models (Figs. 15 and 18). The effects on the BCs are generally too weak, or degenerate with the effects of other parameters, to provide useful constraints. On the other hand, the *R*-band lightcurve provide a constraint on the initial mass, at least as strong as the one obtained from the bolometric lightcurve, and seems to exclude 17 $M_\odot$ models (Fig. 17). This is because the [O I] 6300,6364 Å line, which depends strongly on the initial mass (J14), contributes ∼50 percent of the flux in this band. Furthermore, as the fractional oxygen mass increase with initial mass (J14), both the *R*-band BC and the bolometric luminosity increase with initial mass, making *R*-band photometry particularly useful to constrain the initial mass. The choice of initial mass is motivated by the agreement with nebular spectra (J14) and the optical-to-MIR pseudo-bolometric and *R*-band lightcurves, whereas the choice of macroscopic mixing is motivated by the optical-to-MIR pseudo-bolometric lightcurve.

Density contrast Only significantly affects the BCs. In general the effect on the BCs is small, but there is a strong effect on BC_H at >300 days, caused by the [Si I] 16450 Å line. However, there is a similar effect on BC_H, caused by the positron trapping (see below), and it is not possible to constrain the density contrast alone. Our NIR coverage ends at ∼400 days, but the observed evolution of $BC_{H,P}$ does not favour models with low density contrast and non-local positron trapping (Fig. 19). The choice of a high density contrast is mainly motivated by the agreement with nebular spectra (J14), but is consistent with the oxygen zone filling factor of $\lesssim$0.07, derived from small scale fluctuations in the [O I] 6300,6364 Å and Mg I] 4571 Å lines (Sect. 3.6).

Positron trapping Only significantly affects the BCs. The effect is prominent at late times, when the positrons start to dominate the energy deposition, because locally trapped positrons deposit all their energy in the low temperature Fe/Co/He zone. This results in redder emission, and the luminosity of lines originating from this zone is boosted. Due to this, the optical decline rate is higher at >300 days for models with local trapping, which is in better agreement with observations (Fig. 16). At >400 days, the observed optical decline rate starts to decrease, and models with local positron trapping start to diverge from observations. This could be a sign of additional energy sources (Sect. 5), and is not necessarily in conflict with locally trapped positrons. We find particularly strong line effects in BC_J and BC_H at >300 days, caused by the [Fe II] 12567 Å and [Fe II] 16440 Å lines, respectively. As discussed above, the effect on BC_H is degenerate with a similar effect caused by the density contrast. Our NIR coverage ends at ∼400 days, but the observed evolution of $BC_{J,P}$ seems to be in better agreement with models with local positron trapping (Fig. 19). The choice of local positron trapping is motivated by the optical pseudo-bolometric lightcurve and the evolution of $BC_{J,P}$ at 300−400 days, although the decreasing optical decline rate observed at >400 days is a caveat. The constraints obtained from nebular spectra are not conclusive (J14).

4.1.5. Dust, molecules and the MIR evolution

Some of the most interesting results obtained from the pseudo-bolometric and broad-band lightcurves are related to the MIR evolution and the molecular cooling and dust parameters. There is a strong increase in the fractional MIR luminosity between 100 and 250 days, during which an increase in the decline rate of the optical pseudo-bolometric lightcurve is also observed (Sect. 2). This behaviour is reminiscent of dust formation in the ejecta, and has previously been observed in SN 1987A (Suntzeff & Bouchet 1990). From E14 we know that there is an excess in the S_2-band, as compared to blackbody fits, developing already during the first hundred days. The S_2-band overlaps with the CO fundamental and SiO first-overtone bands, so in this band molecule emission provides an alternative or complementary explanation. CO first-overtone emission is observed at 206 days, and possibly at 89 days (Sect. 3.3), which implies at least some contribution from CO fundamental band emission to the S_2 flux. Below we discuss the constraints on the molecular cooling and dust parameters obtained from the lightcurves, but also additional constraints obtained from spectra not discussed in J14.

Dust Only affects the BCs and tends to decrease the optical emission and increase the *K*-band and MIR emission, as the hot radiation from the SN is absorbed and re-emitted at a lower

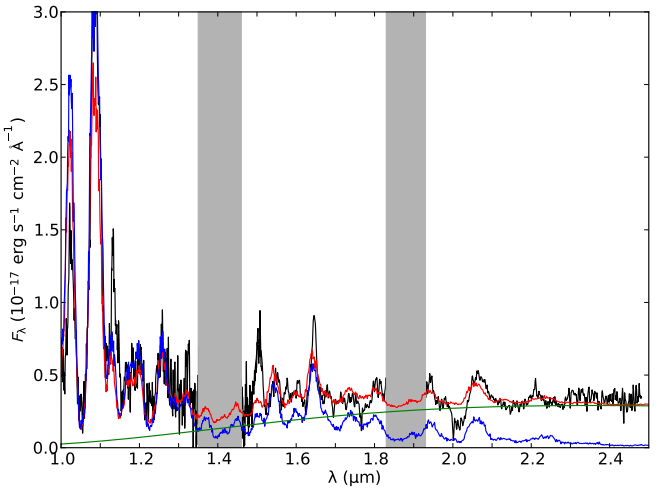

Fig. 20. Observed zJ and HK spectra at 198 and 206 days (black) compared to NIR spectra for the preferred model (12F; red) and model 12E (blue), which differs only in that $\tau_{\rm dust}$=0. The observed spectra were flux calibrated with the interpolated observed J, H and K magnitudes at 200 days and we also show the dust emission component for the preferred model (green).

temperature. CO first-overtone emission contributes negligible to the K-band flux (Sect. 3.3), so the observed excess in this band can be solely attributed to dust emission. As mentioned, models with dust has an opacity in the core, turned on at 200 days, which results in a decrease of the optical BC and a simultaneous increase of BC$_K$ and the MIR BCs. The preferred model (with $\tau_{\rm dust}$=0.44) well reproduces both the drop in the optical pseudo-bolometric lightcurve (Fig. 16) and the increase in BC$_{K,\rm P}$ and BC$_{S_1,\rm P}$ (Fig. 19), whereas the original J14 models (with $\tau_{\rm dust}$=0.25) only qualitatively reproduce this behaviour. This shows, most importantly, that the absorbed and emitted luminosities are in good agreement, and suggests a scenario where the emission arise from nearby, newly formed dust, presumably in the ejecta. Note that the dust contribution is insufficient to reproduce the excess in the S_2-band (Fig. 19), suggesting a contribution from molecule emission in this band (see below).

Further support for a local origin of the emission is gained from spectra. In Fig. 20 we show the observed NIR spectrum at ∼200 days, as compared to NIR spectra for the preferred model and model 12E (same but without dust) at 200 days, as well as the dust emission component for the preferred model. The observed flux at the absorption minimum of the He I 20581 Å line is a factor of ∼2 below the model dust emission level[4], which suggests this emission to originate from $\lesssim$10000 km s^{-1}, and disfavours a thermal echo from heated CSM dust (but see Helou et al. 2013). The small blue-shifts in the [O I] 6300,6364 Å and Mg I] 4571 Å lines at 415 days (Sect. 3.5) and the lack of a physical model for the temperature evolution are caveats though. Regardless of the location, dust emission seems to be required to explain the strong discrepancy between observations and models without dust in the K and S_1 bands (Fig. 19), further illustrated by the spectral comparison in Fig. 20. A MIR excess developing between 100 and 250 days was also observed for SN 1993J (Sect. 2.3). The cause of this excess was suggested by Matthews et al. (2002) to be dust, but the absence of an increase in the optical pseudo-bolometric decline rate indicates that, if this emission is due to dust, it would rather arise from heated CSM dust. Except for SNe 2011dh and 1993J, we have found no reports of dust emission in Type IIb or stripped envelope SNe in the literature.

[4] Note that the model dust emission has not been subject to radiative transfer (Appendix C.4), so the depth of the model He I 20581 Å absorption corresponds to that expected for a thermal echo.

Molecular cooling Only affects the BCs and results in a redistribution of cooling emission from the O/C and O/Si/S zones to the CO and SiO molecular bands. The effect is strong in the S_2-band, which overlaps with the CO fundamental and SiO first-overtone bands, and there is also a significant effect in the K-band, which overlaps partly with the CO first-overtone band. The observed CO first-overtone emission implies some amount of CO cooling at 206 days, and possibly at 89 days, but is ∼2.5 and ∼3.5 mag too faint, respectively, as compared to models with complete molecular cooling. As mentioned, there is an excess in the S_2-band as compared to the preferred model (without molecular cooling), which shows the best agreement for a conceivable dust component. As compared to this model, BC$_{S_2,\rm P}$ is 0.5−1.0 mag to large, but as compared to models with complete molecular cooling, BC$_{S_2,\rm P}$ is ∼2 and 0.5−1.0 mag too small at 85 and >251 days, respectively (Fig. 19). As molecule emission in the S_2-band is likely to be dominated by the CO fundamental band (Appendix C.3), this suggests a small amount of CO cooling at 85 days, increasing to an intermediate amount at >251 days, whereas the observed CO first-overtone emission suggests a small amount of CO cooling at 89 and 206 days.

The interpretation of the CO first-overtone emission and the S_2 excess depends on the fundamental to first-overtone band ratio, which is assumed to be the same as observed in SN 1987A (Appendix C.3). The observed CO first-overtone and S_2 fluxes give an upper limit on this ratio, which can be improved by subtracting a model for the underlying emission, and if we again assume the excess in the S_2-band to be dominated by CO fundamental band emission, we can estimate it. Using the preferred model for the underlying emission, keeping in mind that the S_2 magnitudes have to be interpolated between 85 and 251 days, we get upper limits of 6.8 and 16 and estimates of 4.5 and 7.7 at 89 and 206 days, respectively. These values are significantly larger than in the models (∼1 and ∼2, respectively), and would naively suggest a lower temperature for the CO. So, either the fundamental to first-overtone band ratios are significantly higher than observed in SN 1987A, or the excess in the S_2-band is not caused by CO (but e.g. SiO or heated CSM dust).

Further constraints on the amount of molecular cooling is gained from thermal lines originating in the O/C an O/Si/S zones, in particular the blended Ca II 8498,8542,8662 Å and [C I] 8727 Å lines (J14). The evolution of this blend is reflected in the evolution of the I and z bands, which seems to exclude models with complete molecular cooling at $\lesssim$250 days (Fig. 19; but see also J14), Such models also seem to be excluded at later times due to the (likely) continued presence of the [C I] 8727 Å line (Sect. 3.5). Finally, the remarkable similarity between the [O I] 6300 Å and Mg I] 4571 Å lines, suggests the contributions to the [O I] 6300 Å flux from the O/C and O/Si/S zones to be modest (Sect. 3.4), in turn suggesting a considerable amount of molecular cooling at $\gtrsim$200 days.

We have chosen no molecular cooling for the preferred model, but neither this scenario nor complete molecular cooling shows a satisfactory agreement with observations. However, the constraints obtained are not necessarily inconsistent, and at least in the O/C zone, a small amount of molecular (CO) cooling at ∼100 days, increasing to an intermediate amount at $\gtrsim$250 days, seems reasonable. CO emission has been reported for the Type

Ic SNe 2002ew (Gerardy et al. 2002) and 2007gr (Hunter et al. 2009), but for Type Ib and IIb SNe we have found no reports of CO emission in the literature. There is a feature near 23000 Å in the NIR spectra of SN 1993J (Matthews et al. 2002), that could be interpreted as a modest amount of CO first-overtone emission.

4.2. Hydrodynamical modelling of the <400 days optical-to-MIR pseudo-bolometric lightcurve

B12 presented hydrodynamical modelling of SN 2011dh, that well reproduced the <80 days UV-to-MIR pseudo-bolometric lightcurve presented in E14. In E15 we use a grid of SN models constructed with HYDE and MESA STAR (Paxton et al. 2011, 2013) to fit the <100 days UV-to-MIR pseudo-bolometric lightcurve, and here we use an extended version of this grid to fit the <400 days optical-to-MIR pseudo-bolometric lightcurve. This is the period for which we have full U to S_2 coverage and, except for the additional ~300 days of data, the method allows us to quantify the errors in the derived quantities and the degeneracy of the solution. The stellar models consist of bare helium cores without a hydrogen envelope, which is a sound approximation as long as the optical depth of the hydrogen envelope is $\ll 1$, and the mass low enough not to (appreciable) decelerate the helium core (E15). The original model grid is described in E15 and the extended one summarized in Appendix D, and the model parameters are the helium core mass (M_{He}), the explosion energy (E), and the mass (M_{Ni}) and distribution (Mix_{Ni}) of the ^{56}Ni. The fitting is done by minimization of the square of the relative residuals, giving equal weights to the diffusion phase lightcurve, the early tail lightcurve, the late tail lightcurve and the diffusion phase photospheric velocities.

The optical-to-MIR BC, which is required to fit the observations, is determined from the J14 steady-state NLTE models, and is discussed in more detail in Appendix C.2. At <100 days the BC is likely >−0.15 mag and is assumed to be negligible, and at 100−400 days we take advantage of the small spread (<±0.1 mag) in the model BCs during this period, and use the BC for the preferred steady-state NLTE model. As discussed in Appendix C.2 this is motivated for all hydrodynamical models that could possibly give a good fit to the lightcurve.

The left panels of Fig. 21 show the optical-to-MIR pseudo-bolometric lightcurve and the photospheric velocities for the best-fit model as compared to observations, where the photospheric velocities have been estimated from the absorption minimum of the Fe II 5169 Å line. The right panels of Fig. 21 show contour plots of the standard deviation in the fit, normalized to that of the best-fit model. The fits to the lightcurve and the photospheric velocities are both good, and the solution is well constrained in the E-M_{He} plane (upper right panel). When only the lightcurve is used in the fit (lower right panel), the solution is completely degenerate along the M_{ej}^2/E=const curve, in agreement with the <100 days results in E15. The good fit to the lightcurve suggests that other isotopes than ^{56}Ni and ^{56}Co, or additional energy sources like those discussed in Sect. 5, do not contribute substantially to the luminosity before 400 days.

Table 3 lists the best-fit values for the helium core mass, explosion energy and mass and distribution of the ^{56}Ni. These results are consistent within error bars with those for the <80 and <100 days lightcurves obtained in B12 and E15 (Table 3). The addition of the late-time data seems to decrease the explosion energy and helium core mass slightly, and these are ~10 percent lower as compared to the results obtained in E15. The strong mixing of the ^{56}Ni found (95 percent in mass, see Appendix D),

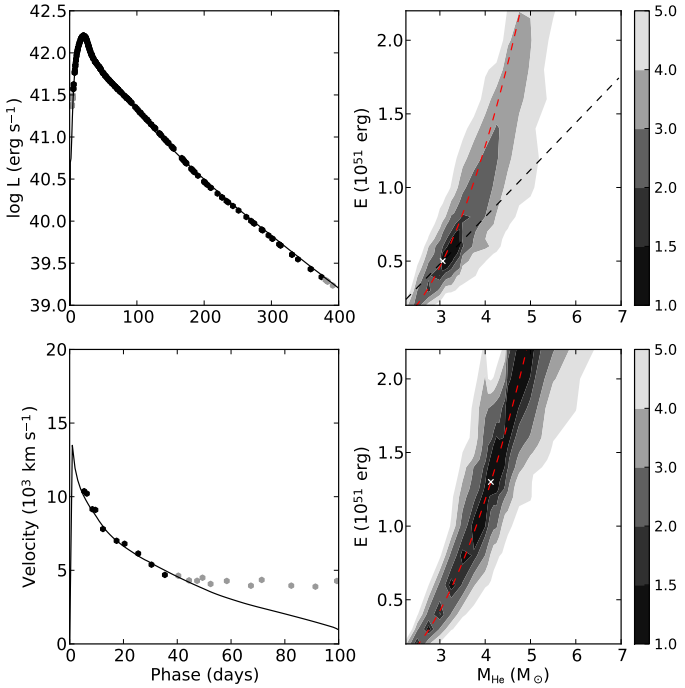

Fig. 21. Left panels: Optical-to-MIR pseudo-bolometric lightcurve (upper left panel) and photospheric velocities (lower left panel) for the best-fit model as compared to observations, where the photospheric velocities have been estimated from the absorption minimum of the Fe II 5169 Å line. Observations not included in the fit are displayed in grey. Right panels: Contour plots showing the (grey-scale coded) standard deviation in the fit, normalized to that of the best-fit model, projected onto the E-M_{He} plane for the case where the photospheric velocities were used (upper right panel) and not used (lower right panel). We also show the constraints M_{ej}/E=const (blue) and M_{ej}^2/E=const (red) provided by the photospheric velocities and the bolometric lightcurve, respectively (E15).

is in good agreement with the results obtained in B12 and E15, and seems to be required to fit the rise to peak luminosity (see also Sect. 4.1.4). The fraction of the ^{56}Ni outside 3500 km s^{-1} is ~50 percent in the best-fit model, and naively this is in contradiction with the small size of the Fe/Co/He line emitting region estimated in Sect. 3.4. However, the amount of high velocity Fe/Co/He material does not necessarily need to be high to reproduce the rise to peak luminosity, and further modelling is needed to resolve this issue. The errors in the distance, extinction and photospheric velocities (where we have assumed a systematic error of 15 percent) have been propagated to the derived quantities, but without taking the degeneracy of the solution into account. However, as is evident from the contour plots, the constraint on the quantity M_{ej}^2/E is strong, and even if the photospheric velocities were considerably *underestimated*, which seem unlikely, a helium core mass of $\gtrsim$4 $M_\odot$ would be excluded.

5. The >500 days lightcurves

As discussed in Sect. 2.3 there is a strong flattening of the observed pseudo-bolometric lightcurves after ~450 days[5], which is also when these start to diverge from the preferred steady-state NLTE model (Sect. 4.1.2). Figure 22 shows the >200 days observed optical-to-MIR, optical-plus-MIR (excluding NIR), optical and MIR pseudo-bolometric lightcurves, as compared to the

[5] Note that there is an observational gap between 467 and 601 days.

Table 3. Helium core mass, explosion energy and mass and distribution of the ^{56}Ni as derived from the <400 days optical-to-MIR pseudo-bolometric lightcurve in this work, and from the <80 and <100 days UV-to-MIR pseudo-bolometric lightcurves in B12 and E15, respectively. The mass of the ^{56}Ni given in B12 has been adjusted with respect to the distance and extinction (E14).

Reference	M_{He} ($M_\odot$)	E (erg)	M_{Ni} ($M_\odot$)	Mix_{Ni}
This work	3.06 (+0.68,-0.44)	0.50 (+0.42,-0.22)	0.075 (+0.028,-0.020)	0.95 (+0.06,-0.04)
E15	3.31 (+0.54,-0.57)	0.55 (+0.35,-0.28)	0.075 (+0.028,-0.020)	1.05 (+0.08,-0.00)
B12	3.3-4.0	0.6-1.0	0.06-0.10	0.95

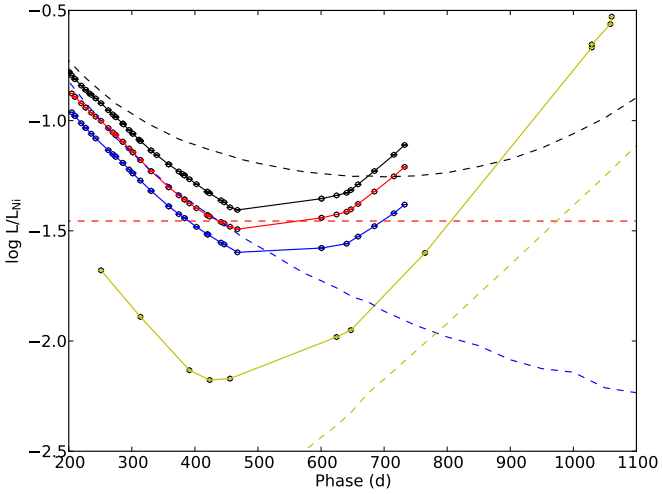

Fig. 22. The >200 days optical-to-MIR (black dots), optical-plus-MIR (red dots), optical (blue dots) and MIR (yellow dots) pseudo-bolometric lightcurves, as compared to the bolometric lightcurve (black dashed line), deposited ^{56}Co γ-ray (blue dashed line) and positron (red dashed line) luminosity and deposited ^{57}Co luminosity (yellow dashed line) for the preferred steady-state NLTE model (12F). The lightcurves have been normalized to the radioactive decay chain luminosity of 0.075 $M_\odot$ of ^{56}Ni.

bolometric lightcurve, deposited ^{56}Co γ-ray and positron luminosity and deposited ^{57}Co luminosity for the preferred steady-state NLTE model[6]. As is clear from the figure, the deposited ^{56}Co luminosity is dominated by the positron contribution after ∼450 days, and the observed $\gtrsim$600 days lightcurves are unlikely to be powered by the γ-rays emitted in the ^{56}Co decay. Shivvers et al. (2013) suggested that the SN entered a phase powered by the positrons emitted in the ^{56}Co decay after 300−350 days. Given our results, this suggestion seems to be roughly correct in the sense that the positron contribution dominates the deposited luminosity after ∼450 days. However, as we discuss below, there is evidence for additional energy sources and the positron contribution does not seem to dominate the emitted luminosity.

The J14 models were not evolved beyond 500 days as the steady-state condition is no longer valid (see below). However, a similar set of models, which were evolved to 700 days, all show a decrease in the optical and optical-to-MIR BCs after 500 days, corresponding to redder emission. This decrease is particularly strong for models with local positron trapping due to the increasing contribution from the low temperature Fe/Co/He zone. Assuming that the actual BCs behave similarly and do not increase, the $\gtrsim$600 days pseudo-bolometric decline rates, which becomes significantly lower than the decay rate of ^{56}Co (Sect. 2.3), are not consistent with a model powered by this decay. Furthermore, assuming again that the actual BCs do not increase, the actual bolometric luminosity at 732 days would be $\gtrsim$0.6 mag higher than the radioactive energy deposition in the preferred model. Even if we ignore the BCs, the observed optical-plus-MIR luminosity at 732 days equals the radioactive energy deposition in the preferred model, and the observed MIR luminosity at 1061 days is 1.1 mag higher. So both the observed decline rates and the observed luminosities suggest that additional energy sources are required to power the $\gtrsim$600 days lightcurves.

If the recombination time scales become longer than the time scale of the ^{56}Co decay, some fraction of the energy is deposited in a growing ionization reservoir, which through recombination emission could eventually dominate the emitted luminosity. This process, called freeze-out, is an example of time-dependent effects that might violate the steady-state assumption in late phases. We use a time-dependent NLTE code (Kozma & Fransson 1992, 1998a,b) to test this assumption, and find that time-dependent effects begin to become important at ∼600 days, and after ∼800 days they provide a dominant and increasing contribution to the optical flux. In the particular model tested, which is similar to the preferred model, this contribution is not sufficient to reproduce the observed lightcurves. However, due to clumping or asymmetries, low density components may exist in the ejecta, for which freeze-out would occur earlier. The 678 day spectrum of SN 2011dh presented by Shivvers et al. (2013), shows features not present in our last optical spectra that *could* be identified as the He I 6678 Å and 7065 Å lines, whereas the strong feature identified as Na I 5890,5896 Å by the authors *could* have a significant contribution from, or be fed by, the He I 5876 Å line. This is consistent with a contribution from recombination emission due to freeze-out in the helium envelope.

CSM interaction became the dominant energy source at ∼300 days for SN 1993J, giving rise to broad box-like Hα and Na I 5890,5896 Å lines and a considerable flattening of the lightcurves. The 678 day spectrum of SN 2011dh shows a feature that Shivvers et al. (2013) interpret as broad box-like Hα emission, but no broad box-like Na I 5890,5896 Å emission is seen. The interpretation of the broad feature as Hα emission is far from clear, as a number of other lines may contribute in this wavelength range (including the [N II] 6548,6583 Å line discussed in Sect. 3.2 and the He I 6678 Å line mentioned above), and the feature is much weaker than for SN 1993J at a similar epoch. Additional energy could also be provided by the decay of radioactive isotopes other than ^{56}Co. In the preferred steady-state NLTE model, the fractional bolometric luminosity deposited by the ^{57}Co decay is ∼10 percent at 700 days and increasing. A higher mass of ^{57}Co would help explain the observed evolution and can not be excluded. A thermal echo

[6] These were calculated with HYDE using the same ejecta model as the preferred steady-state NLTE model.

from heated CSM dust could possibly power the MIR pseudo-bolometric lightcurve, but can not explain the behaviour of the optical pseudo-bolometric lightcurve. Another possibility is that the observed flux does not solely originates from the SN, but this seems to be ruled out by the 678 day spectrum, which is line dominated and has a minimum flux level close to zero. In summary, we find observational and theoretical evidence that the contribution from the positrons emitted in the ^{56}Co decay does not dominate the observed $\gtrsim$600 days luminosity. A substantial contribution from time-dependent effects is likely, whereas contributions from other energy sources can not be excluded.

6. Conclusions

We present the post 100 days part of our optical and NIR, photometric and spectroscopic dataset for the Type IIb SN 2011dh. The dataset spans two years, and together with SWIFT and Spitzer observations it covers the UV to MIR wavelength range. Particular attention is paid to the pseudo-bolometric and broad-band lightcurves, where we use steady-state NLTE modelling and hydrodynamical modelling to put constraints on the SN and progenitor parameters.

We analyse the <400 days optical-to-MIR pseudo-bolometric lightcurve of SN 2011dh, using a grid of hydrodynamical SN models and a optical-to-MIR BC determined with steady-state NLTE modelling. Using this method we find model parameters consistent within error bars with those obtained in B12 using the <80 days UV-to-MIR pseudo-bolometric lightcurve. In particular, we find a helium core mass of $3.1^{+0.7}_{-0.4}$ $M_\odot$ which, taking into account also the degeneracy of the solution, gives upper limits on the helium core and initial mass of $\lesssim$4 $M_\odot$ and $\lesssim$15 $M_\odot$, respectively.

We analyse the 100−500 days pseudo-bolometric and broad-band lightcurves of SN 2011dh, using the set of steady-state NLTE models presented in J14. The preferred 12 $M_\odot$ (initial mass) model, refined in this work with respect to the dust, shows an overall agreement with the observed broad-band and pseudo-bolometric lightcurves. In particular, the simultaneous increase in the optical pseudo-bolometric decline rate and the fractional K and S_1 luminosities between 100 and 250 days is reproduced by this model, which has a modest dust opacity in the core ($\tau_{\rm dust}$ = 0.44), turned on at 200 days. A local origin of the excess emission is supported by the depth of the He I 20581 Å absorption. We find the dust contribution insufficient to reproduce the S_2 magnitudes and, assuming this additional excess to be dominated by CO fundamental band emission, an intermediate amount of CO cooling in O/C zone is likely. This is consistent with the detected CO first-overtone emission, although the fundamental to first-overtone band ratios needs to be significantly higher than observed in SN 1987A.

The >500 days lightcurves have not been systematically modelled, but there is both observational and theoretical evidence that the SN becomes powered by additional energy sources in this phase. At >400 days the optical and MIR pseudo-bolometric lightcurves flatten to fast, and at >600 days their luminosities become too high, to be powered by the radioactive energy deposition. Modelling with a time-dependent NLTE code (Kozma & Fransson 1992, 1998a,b) shows that time-dependent effects become important at ∼600 days, after which a steady-state assumption is no longer valid, and after ∼800 days they provide a dominant and increasing contribution to the optical luminosity. We find substantial contributions from CSM interaction and other radioactive isotopes less likely, whereas a substantial contribution from coincident sources is ruled out.

We estimate progressively smaller sizes, ranging from ∼3000 to ∼1500 km s^{-1}, for the line emitting regions of oxygen, magnesium, [Ca II] 7291,7323 Å and iron. These regions correspond to the oxygen, O/Ne/Mg, Si/S and Fe/Co/He nuclear burning zones (J14), and suggest incomplete mixing of the core material. The profiles of the [O I] 6300 Å and Mg I] 4571 Å lines show a remarkable similarity, suggesting these lines to arise from the O/Ne/Mg zone. We use repetitions of small scale fluctuations in the [O I] 6300 Å and 6364 Å lines to find a line ratio close to 3, consistent with optically thin emission, from 200 days and onwards. Applying the method of Chugai (1994) to these small scale fluctuations, we find an upper limit on the filling factor for the [O I] 6300 Å and Mg I] 4571 Å line emitting material of ∼0.07, and a lower limit on the number of clumps of ∼900.

This paper concludes our work on SN 2011dh presented in M11, E14 and J14. In addition, modelling of our data have been presented by B12. We have applied stellar evolutionary progenitor analysis, hydrodynamical modelling, SN atmosphere modelling and steady-state NLTE modelling to our extensive set of observational data. Although a number of issues remain unsolved, the main characteristics of the SN and its progenitor star found by the different methods are consistent. The progenitor star appears to have been of moderate ($\lesssim$15 $M_\odot$) initial mass, and the 3−4 $M_\odot$ helium core surrounded by a low-mass (∼0.1 $M_\odot$) and extended (200−300 $R_\odot$) hydrogen envelope. Given the upper bound on the initial mass of ∼15 $M_\odot$, the mass-loss rate is probably not strong enough to expel the hydrogen envelope before core-collapse, and a binary origin for SN 2011dh is suggested. Folatelli et al. (2014) find a blue source they suggest to be the companion star in HST UV imaging obtained at ∼1200 days, but it is unclear how they can exclude a contribution from the SN, and further work is likely needed to settle this issue.

7. Acknowledgements

This work is based on observations obtained with the Nordic Optical Telescope, operated by the Nordic Optical Telescope Scientific Association at the Observatorio del Roque de los Muchachos, La Palma, Spain, of the Instituto de Astrofisica de Canarias; the German-Spanish Astronomical Center, Calar Alto, jointly operated by the Max-Planck-Institut für Astronomie Heidelberg and the Instituto de Astrofísica de Andalucía (CSIC); the United Kingdom Infrared Telescope, operated by the Joint Astronomy Centre on behalf of the Science and Technology Facilities Council of the U.K.; the William Herschel Telescope and its service programme (proposals SW2011b21 and SW2012a02), operated on the island of La Palma by the Isaac Newton Group in the Spanish Observatorio del Roque de los Muchachos of the Instituto de Astrofisica de Canarias; the Copernico 1.82m Telescope and Schmidt 67/92 Telescope operated by INAF - Osservatorio Astronomico di Padova at Asiago, Italy; by the 3.6m Italian Telescopio Nazionale Galileo operated by the Fundación Galileo Galilei - INAF on the island of La Palma; the Liverpool Telescope, operated on the island of La Palma by Liverpool John Moores University in the Spanish Observatorio del Roque de los Muchachos of the Instituto de Astrofisica de Canarias with financial support from the UK Science and Technology Facilities Council; the AlbaNova telescope operated by the Department of Astronomy at Stockholm University and funded by a grant from the Knut and Alice Wallenberg Foundation; the Gran Telescopio Canarias (GTC), installed in the Spanish Observatorio del Roque de los Muchachos of the Instituto de Astrofísica de Canarias, in the island of La Palma. We acknowledge the exceptional support

we got from the NOT staff throughout this campaign, we thank the Calar Alto Observatory for allocation of director's discretionary time and we thank Philip Dufton, Paul Dunstall, Darryl Wright and Lindsay Magill for assistance with the WHT observations.

The Oskar Klein Centre is funded by the Swedish Research Council. J.S. acknowledge support by the Swedish Research Council. S.J.S. thanks European Research Council under the European Union's Seventh Framework Programme (FP7/2007-2013)/ERC Grant agreement n^{o} [291222] and STFC. A.P., L.T. and S.B. are partially supported by the PRIN-INAF 2011 with the project "Transient Universe: from ESO Large to PESSTO". M.F. acknowledges support by the European Union FP7 programme through ERC grant number 320360. N.E.R. acknowledges the support from the European Union Seventh Framework Programme (FP7/2007-2013) under grant agreement n^{o} 267251 "Astronomy Fellowships in Italy" (AstroFIt). R.K. acknowledges observing time at the LT, NOT, TNG, and WHT via programme CCI-04. M.M.K. acknowledges generous support from the Hubble Fellowship and Carnegie-Princeton Fellowship.

We thank Melina Bersten for providing the post-explosion density profile for the He4R270 model (B12), for inspiration and a great contribution to the understanding of SN 2011dh. We thank Peter Meikle and Dan Milisavljevic for providing spectra on SN 1993J and SN 2008ax, respectively.

Appendix A: Data reductions and calibration

The reductions and calibration procedures are mostly the same as described in E14. Here we discuss issues specifically related to the >100 days data.

Appendix A.1: Template subtraction - 100−500 days optical and NIR observations

Comparison of photometry on the original images and on template subtracted images, shows that the background contamination is negligible before ∼300 days, after which we have used photometry on template subtracted images. The optical templates were constructed by point spread function (PSF) subtraction of the SN from observations acquired after 600 days, and the NIR templates by PSF subtraction of the SN from the 339 days WHT observation, which is of excellent quality. For the last 380 days WHT observation we used PSF photometry.

Appendix A.2: S-corrections - 100−500 days optical and NIR observations

The accuracy of the late-time photometry depends critically on the accuracy of the S-corrections. Figure A.1 shows the difference between colour and S-corrections for the Johnson-Cousins (JC) and 2 Micron All Sky Survey (2MASS) systems for most telescope/instrument combinations used, and S-corrections are clearly necessary for accurate photometry. In some cases, e.g. for the CA-2.2m/CAFOS and NOT/ALFOSC *I* band and the CA-3.5m/O2000 *J* band, the differences become as large as 0.3−0.5 mag. In particular, the difference between the NOT/ALFOSC and CA-2.2m/CAFOS *I* band observations are ∼0.8 mag at ∼250 days, mainly due to the strong [Ca II] 7291,7323 Å and Ca II 8498,8542,8662 Å lines. As the spectral NIR coverage ends at ∼200 days, we have assumed that the 2MASS S-corrections do not change during the 200−400 days period. This adds uncertainty to the 2MASS photometry after ∼200 days, but as the 2MASS S-corrections, except for the CA-3.5m/O2000 *J* band, are generally small and evolve slowly, the errors arising from this approximation are probably modest. The accuracy of the S-corrections can be estimated by comparing S-corrected photometry obtained with different telescope/instrument combinations. The late-time JC and Sloan Digital Sky Survey (SDSS) photometry were mainly obtained with the NOT, but comparisons between S-corrected NOT/ALFOSC, LT/RATCam and CA-2.2m/CAFOS photometry at ∼300 days, show differences at the 5 percent level, suggesting that the precision from the <100 days period is maintained (E14). The late-time 2MASS photometry was obtained with a number of different telescopes, and although the sampling is sparse, the shape of the lightcurves suggests that the errors in the S-corrections are modest. Additional filter response functions for AT and UKIRT have been constructed as outlined in E14.

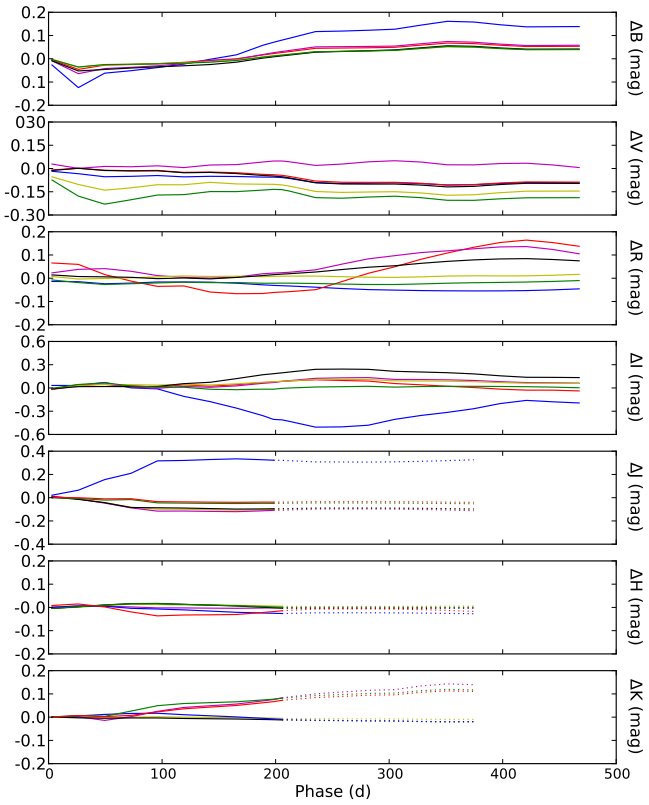

Fig. A.1. Difference between JC *BVRI* colour and S-corrections for NOT/ALFOSC (black), LT/RATCam (red), CA-2.2m/CAFOS (blue), TNG/LRS (green), AS-1.82m/AFOSC (yellow) and AS-Schmidt (magenta), and difference between 2MASS *JHK* colour and S-corrections for NOT/NOTCAM (black), TCS/CAIN (red), CA-3.5m/O2000 (blue), TNG/NICS (green), WHT/LIRIS (yellow) and UKIRT/WFCAM (magenta). Results based on extrapolated 2MASS S-corrections are shown as dotted lines.

Appendix A.2.1: Post 600 days optical observations

The results for the post 600 days observations have been adopted from the pre-explosion difference imaging presented in E14, assuming that the remaining flux at the position of the progenitor originates solely from the SN. The observations were S-corrected using the 678 day spectrum of SN 2011dh (Shivvers et al. 2013). Comparing to results from PSF photometry, where

we iteratively fitted the PSF subtracted background, we find differences of $\lesssim$0.1 mag. Given that the pre-explosion magnitudes (which were measured with PSF photometry) are correctly measured, the difference based magnitudes are likely to have less uncertainty. On the other hand, the PSF photometry does not depend on the the pre-explosion magnitudes. The good agreement found using these two, partly independent methods gives confidence in the results. Further confidence is gained by comparing the S-corrected NOT and HST (Van Dyk et al. 2013) V-band observations, for which we find a difference of $\lesssim$0.2 mag. The assumption that the flux at the position of the progenitor originates solely from the SN, is supported by the the depth of absorption features and the line dominated nature of the 678 days spectrum.

Appendix A.2.2: Spitzer Telescope observations

For the >100 days photometry we used a small aperture with a 3 pixel radius, and a correction to the standard aperture given in the IRAC Instrument Handbook determined from the images. All images were template subtracted using archival images as described in (E14). After 100 days, background contamination becomes important, and template subtraction is necessary to obtain precision in the photometry. The <700 days photometry previously published by Helou et al. (2013) agrees very well with our photometry, the differences being mostly $\lesssim$5 percent.

Appendix B: Line measurements

Appendix B.1: Line emitting regions

To estimate the sizes of the line emitting regions, we fit the line profile of a spherically symmetric region of constant line emissivity, optically thin in the line (no line scattering contribution) and with a constant absorptive continuum opacity, to the observed, continuum subtracted (Appendix B.3) line profile. The fitting is done by an automated least-square based algorithm, and the method gives a rough estimate of the size of the region responsible for the bulk of the line emission. The absorptive continuum opacity is included to mimic blue-shifts caused by obscuration of receding-side emission. Some lines arise as a blend of more than one line, which has to be taken into account. The [O I] 6300 Å flux was calculated by iterative subtraction of the [O I] 6364 Å flux, from the left to the right, using $F_{6300}(\lambda) = F_{6300,6364}(\lambda) - F_{6300}(\lambda - \Delta\lambda)/R$, where $\Delta\lambda$ is the wavelength separation between the [O I] 6300 Å and 6364 Å lines and R the [O I] 6300,6364 Å line ratio. This ratio was assumed to be 3, as is supported by the preferred J14 steady-state NLTE model and estimates based on small scale fluctuations in the line profiles (Sect. 3.6). For all other blended lines, we make a simultaneous fit with the line ratios as free parameters, assuming a common size of the line emitting regions.

Appendix B.2: Line asymmetries

To estimate the asymmetry of a line we calculate the first wavelength moment of the flux (center of flux) for the continuum subtracted (Appendix B.3) line profile. The rest wavelength is assumed to be 6316 Å and 7304 Å for the [O I] 6300,6364 Å and [Ca II] 7291,7323 Å lines, respectively. This is appropriate for optically thin emission if we assume the upper levels of the [Ca II] 7291,7323 Å line to be populated as in local thermal equilibrium (LTE). Optically thin emission for these lines is supported by the preferred J14 steady-state NLTE model, the absence of absorption features in the observed spectra and the [O I] 6300,6364 Å line ratio (Sect. 3.6). The rest wavelength is assumed to be 5896 Å and 8662 Å for the Na I 5890,5896 Å and Ca II 8498,8542,8662 Å lines, respectively. This is appropriate for optically thick emission, where the line emission will eventually scatter in the reddest line. Optically thick emission for the Na I 5896 Å line is supported by the preferred J14 steady-state NLTE model and the observed P-Cygni profile. For the Ca II 8662 Å line this assumption is less justified.

Appendix B.3: Continuum subtraction

Before fitting the line emitting region or calculating the center of flux, the continuum is subtracted. The flux is determined by a linear interpolation between the minimum flux on the blue and red sides of the smoothed line profile. The search region is set to $\pm$6000 km s^{-1} for most of the lines, $\pm$10000 km s^{-1} for the Ca II 8662 Å line and $\pm$3000 km s^{-1} for the [Fe II] 7155 Å line.

Appendix B.4: Small scale fluctuations

To remove the large scale structure from a line profile we iteratively (3 times) subtract a 1000 km s^{-1} box average. This method has been tested on the product of synthetic large and small scale structures, and the small scale structure is recovered with reasonable accuracy. Using a Monte-Carlo (MC) analogue of the Chugai (1994) model the spatial (relative) RMS of the recovered small scale structure is found to agree well with the actual (relative) RMS of the fluctuations (δ_F in Chugai 1994, eq. 11)).

Appendix C: Steady-state NLTE modelling.

Appendix C.1: Effects of the model parameters

To analyse the effects of the model parameters on the model lightcurves, a split into a bolometric lightcurve and a bolometric correction (BC) is convenient. In terms of these quantities, the broad-band and pseudo-bolometric[7] magnitudes are given by $M = M_{Bol} - BC$. This split is most useful as the bolometric lightcurve depends only on the energy deposition[8], whereas the BCs depend on how this energy is processed. The energy deposition is independent of molecular cooling and dust and, within the parameter space covered by the J14 models, only weakly dependent on the density contrast and the positron trapping. Therefore, the bolometric lightcurves depend significantly only on the initial mass and the macroscopic mixing, whereas the other parameters only significantly affect the BCs. Figures C.1 and C.2 shows the pseudo-bolometric and broad-band BCs for the J14 models. The optical-to-MIR BCs show small differences whereas the optical and, in particular, the broad-bands BCs, show considerably larger differences, which makes them well suited to constrain the model parameters. The bolometric lightcurves (not shown) could as well be calculated with HYDE, and their dependence on the initial mass and macroscopic mixing is better investigated with the hydrodynamical model grid.

Appendix C.2: The optical-to-MIR BC

The optical-to-MIR BCs for the J14 models show small differences (<$\pm$0.1 mag) during the 100−400 days period, which subsequently increase towards $\pm$0.25 mag at 500 days. At 100 days

[7] Pseudo-bolometric luminosity expressed in bolometric magnitudes.
[8] Ignoring the <0.05 mag lost due to scattering in the ejecta.

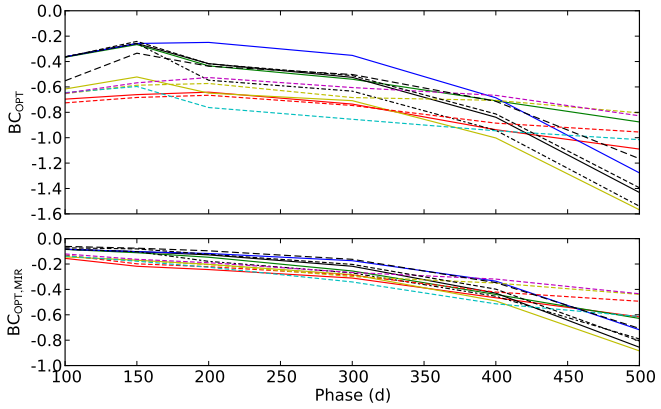

Fig. C.1. 100−500 days optical (upper panel) and optical-to-MIR (lower panel) BCs for the J14 models. The models are displayed as follows; 12A (red solid line), 12B (green solid line), 12C (black solid line), 12D (yellow solid line), 12E (blue solid line), 12F (black dashed-dotted line), 13A (red short-dashed line), 13C (yellow short-dashed line), 13D (cyan short-dashed line), 13E (magenta short-dashed line), 13G (black short-dashed line), 17A (black long-dashed line).

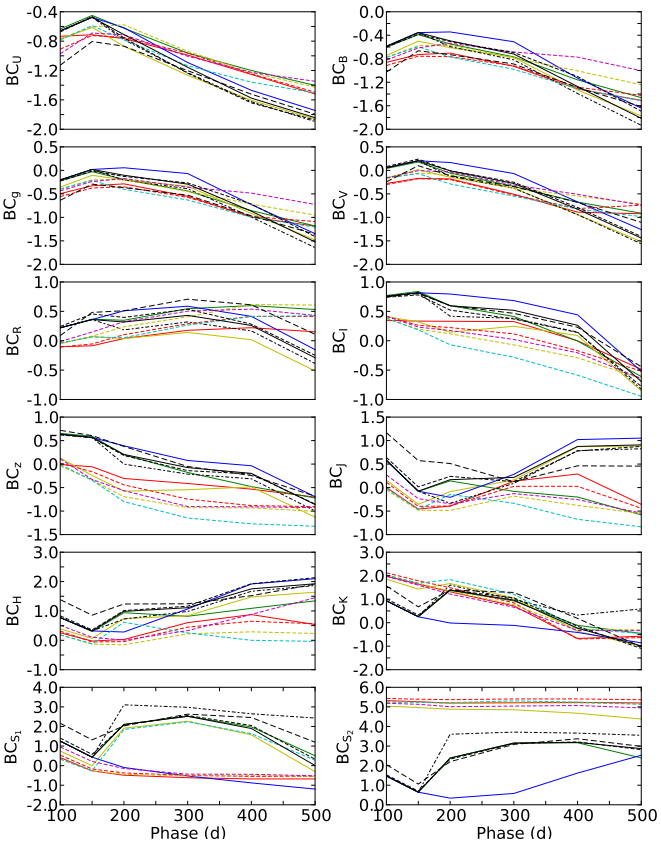

Fig. C.2. 100−500 days broad-band BCs for the J14 models. The models are displayed as in Fig. C.1.

the optical-to-MIR BC is >−0.15 mag, which is likely to hold at <100 days as well. In Sect. 4.2 we take advantage of these facts and use the 100−400 days optical-to-MIR BC for the preferred model for all hydrodynamical models. However, as the J14 models cover a restricted volume of parameter space as compared to the hydrodynamical model grid, we need to justify this choice further. It is reasonable to assume that the BC depends mainly on the energy deposition per unit mass (determining the heating rate) and the density (determining the cooling rate). Furthermore, we know beforehand, that hydrodynamical models giving a bad <100 days fit will not give a good <400 days fit. Inspecting the J14 models and the hydrodynamical models with a normalized standard deviation in the <100 days fit less than 3, we find that these hydrodynamical models do not span a wide range in (mass averaged) density or energy deposition per mass, and that the J14 models cover about half of this region. Although these quantities evolve quite strongly with time, they scale in a similar way for all models, and this conclusion holds for the full 100−400 days period. The effect of the steady-state NLTE parameters that do not map onto the hydrodynamical parameter space (dust, molecular cooling, positron trapping and density contrast) is harder to constrain. The small spread in the BC for the J14 models during the 100−400 days period, make this caveat less worrying though.

Appendix C.3: Treatment of molecular cooling

Molecular cooling is included in the modelling in a simplified way, and is represented as the fraction of the (radiative and radioactive) heating emitted as molecule (CO and SiO) emission in the O/C and O/Si/S zones. The CO and SiO fundamental and first-overtone band emission is represented as box line profiles between 2.25−2.45 (CO first-overtone), 4.4−4.9 (CO fundamental) and 4.0−4.5 (SiO first-overtone) μm. The CO first-overtone band overlaps partly with the K-band, and the CO fundamental and SiO first-overtone bands overlap with the S_2-band, whereas the SiO fundamental band lies outside the U to S_2 wavelength range. The fundamental to first-overtone band flux ratios are assumed to be the same as observed for CO in SN 1987A (Bouchet & Danziger 1993). We have used two configurations, one where the fraction of the heating emitted as molecule emission has been set to one, and one where this fraction has been set to zero. Note that CO fundamental band emission dominates the contribution to the S_2-band in all models at all times. This is because the O/Si/S to O/C zone mass ratio and the CO and SiO fundamental to first-overtone band ratios are all $\lesssim$1, decreasing with increasing initial mass and with time, respectively.

Appendix C.4: Treatment of dust

Dust is included in the modelling in a simplified way, and is represented as a grey absorptive opacity in the core. The absorbed luminosity is re-emitted as blackbody emission with a temperature determined from fits to the photometry. The dust emission is treated separately from the modelling, and is added by post-processing of the model spectra. All the models presented in J14 have the same optical depth and dust temperature, determined from the pseudo-bolometric optical lightcurve and fits to the H, K and S_1 photometry, as described below. In addition we have constructed two new models, 12E which differs from 12C only in the absence of dust and 12F, which differs from 12C only in the optical depth and the method to determine the temperature.

The J14 models have an optical depth of 0.25, turned on at 200 days, which approximately match the behaviour of the optical pseudo-bolometric lightcurve. The temperature is constrained to scale as for a homologously expanding surface, representing a large number of optically thick dust clouds (J14). Minimizing the sum of squares of the relative flux differences of model and observed H, K and S_1 photometry at 200, 300 and 400 days (including H only at 200 days), we find temperatures of 2000, 1097 and 668 K at 200, 300 and 400 days, respectively, given the constraint $T_{dust} < 2000$ K. The S_2-band was excluded

as this band might have a contribution from molecule emission, whereas we know that the contribution from CO first-overtone emission to the K-band at 206 days is negligible. However, the fractional area of the emitting surface (x_{dust}), turns out to be ∼20 times smaller than the fractional area needed to reproduce the optical depth, so the derived temperature is not consistent with the assumptions made.

Model 12F has an optical depth of 0.44, turned on at 200 days, which better match the behaviour of the optical pseudo-bolometric lightcurve. The constraint on the temperature evolution used for the J14 models has been abandoned, and fitting the H, K and S_1 photometry as described above, we find temperatures of 1229, 931 and 832 K at 200, 300 and 400 days respectively. This shows that, in addition to the inconsistency between the absorbing and emitting area, the scaling of temperature is not well reproduced by the J14 models. Due to the better reproduction of the optical pseudo-bolometric lightcurve, and the problems with the temperature scaling used for the J14 models, we use model 12F, instead of model 12C, as our preferred model in this paper. Abandoning all attempts to physically explain the temperature, leaves us with black box model, parametrized with the optical depth and the temperature. This is a caveat, but also fair, as the original model is not self-consistent. Note that the good spectroscopic agreement found for model 12C in J14 does not necessarily apply to model 12F. However, for lines originating from the core, which are expected to be most affected by the higher optical depth of the dust, the flux would be ∼17 percent lower and the blue-shifts ∼100 km s^{-1} higher (Sect. 3.5), so the differences are likely to be small.

Appendix D: HYDE and the model grid

Here we provide a summary of HYDE and the grid of SN models constructed with this code and MESA STAR (Paxton et al. 2011). A detailed description is provided in E15, where we also provide tests of HYDE and a detailed analysis of the behaviour of the model grid.

HYDE Is a one-dimensional Lagrangian hydrodynamical code based on the flux limited diffusion approximation, following the method described by Falk & Arnett (1977), and adopting the flux limiter given by Bersten et al. (2011). The opacity is calculated from the OPAL opacity tables (Iglesias & Rogers 1996), complemented with the low temperature opacities given by Alexander & Ferguson (1994). In addition we use an opacity floor set to 0.01 cm^2 gram^{-1} in the hydrogen envelope and 0.025 cm^2 gram^{-1} in the helium core, following Bersten et al. (2012, private communication), who calibrated these values by comparison to the STELLA hydrodynamical code (Blinnikov et al. 1998). The electron density, needed in the equation of state, is calculated by solving the Saha equation using the same atomic data as in Jerkstrand et al. (2011, 2012). The transfer of the gamma-rays and positrons emitted in the decay chain of ^{56}Ni is calculated with a Monte-Carlo method, using the same grey opacities, luminosities and decay times as in Jerkstrand et al. (2011, 2012).

The model grid Is based on non-rotating solar metallicity helium cores, evolved to the verge of core-collapse with MESA STAR (Paxton et al. 2011). The configuration used was the default one, and a central density limit of $10^{9.5}$ gram cm^{-3} was used as termination condition. The evolved models spans M_{He}=4.0−5.0 $M_\odot$ in 0.25 $M_\odot$ steps and M_{He}=5.0−7.0 $M_\odot$ in 0.5 $M_\odot$ steps. Below 4.0 $M_\odot$, stellar models were constructed by a scaling of the 4.0 $M_\odot$ density profile. The SN explosion was parametrized with the injected explosion energy (E), the mass of the ^{56}Ni (M_{Ni}) and the distribution of it. The mass fraction of ^{56}Ni (X_{Ni}) was assumed to be a linearly declining function of the ejecta mass (m_{ej}) becoming zero at some fraction of the total ejecta mass (Mix_{Ni}), expressed as $X_{Ni} \propto 1 - m_{ej}/(Mix_{Ni}M_{ej}), X_{Ni} \geq 0$. Note that this expression allows $Mix_{Ni} > 1$, although the interpretation then becomes less clear. The total volume of parameter space spanned is M_{He}=2.5−7.0 $M_\odot$, E=0.2−2.2×10^{51} erg, M_{Ni}=0.015−0.250 $M_\odot$ and Mix_{Ni}=0.6−1.6 using a 12×16×13×9 grid. A mass cut with zero velocity was set at 1.5 $M_\odot$, the material below assumed to form a compact remnant, although fallback of further material onto this boundary is not prohibited. To calculate 100−400 days bolometric lightcurves we run HYDE in homologous mode, ignore the radiative transfer, and take the bolometric luminosity as the deposited radioactive decay energy (Appendix C.1).

References

Alexander, D. R. & Ferguson, J. W. 1994, ApJ, 437, 879
Arcavi, I., Gal-Yam, A., Yaron, O., et al. 2011, ApJ, 742, L18
Benvenuto, O. G., Bersten, M. C., & Nomoto, K. 2013, ApJ, 762, 74
Bersten, M. C., Benvenuto, O., & Hamuy, M. 2011, ApJ, 729, 61
Bersten, M. C., Benvenuto, O. G., Nomoto, K., et al. 2012, ApJ, 757, 31
Blinnikov, S. I., Eastman, R., Bartunov, O. S., Popolitov, V. A., & Woosley, S. E. 1998, ApJ, 496, 454
Bouchet, P. & Danziger, I. J. 1993, A&A, 273, 451
Chugai, N. N. 1994, ApJ, 428, L17
Ergon, M., Sollerman, J., Fraser, M., et al. 2014, A&A, 562, A17
Ergon, M., Sollerman, J., Jerkstrand, A., & Fransson, C. 2015, In preparation
Falk, S. W. & Arnett, W. D. 1977, ApJS, 33, 515
Filippenko, A. V. & Sargent, W. L. W. 1989, ApJ, 345, L43
Folatelli, G., Bersten, M. C., Benvenuto, O. G., et al. 2014, ApJ, 793, L22
Fox, O. D., Azalee Bostroem, K., Van Dyk, S. D., et al. 2014, ArXiv e-prints
Gerardy, C. L., Fesen, R. A., Nomoto, K., et al. 2002, PASJ, 54, 905
Griga, T., Marulla, A., Grenier, A., et al. 2011, Central Bureau Electronic Telegrams, 2736, 1
Helou, G., Kasliwal, M. M., Ofek, E. O., et al. 2013, ApJ, 778, L19
Hunter, D. J., Valenti, S., Kotak, R., et al. 2009, A&A, 508, 371
Iglesias, C. A. & Rogers, F. J. 1996, ApJ, 464, 943
Iwamoto, K., Young, T. R., Nakasato, N., et al. 1997, ApJ, 477, 865
Jerkstrand, A., Ergon, M., Smartt, S., et al. 2014, In preparation
Jerkstrand, A., Fransson, C., & Kozma, C. 2011, A&A, 530, A45
Jerkstrand, A., Fransson, C., Maguire, K., et al. 2012, A&A, 546, A28
Kozma, C. & Fransson, C. 1992, ApJ, 390, 602
Kozma, C. & Fransson, C. 1998a, ApJ, 496, 946
Kozma, C. & Fransson, C. 1998b, ApJ, 497, 431
Lavaux, G. & Hudson, M. J. 2011, MNRAS, 416, 2840
Matheson, T., Filippenko, A. V., Ho, L. C., Barth, A. J., & Leonard, D. C. 2000, AJ, 120, 1499
Matthews, K., Neugebauer, G., Armus, L., & Soifer, B. T. 2002, AJ, 123, 753
Maund, J. R., Fraser, M., Ergon, M., et al. 2011, ApJ, 739, L37
Maund, J. R., Smartt, S. J., Kudritzki, R. P., Podsiadlowski, P., & Gilmore, G. F. 2004, Nature, 427, 129
Milisavljevic, D., Fesen, R. A., Gerardy, C. L., Kirshner, R. P., & Challis, P. 2010, ApJ, 709, 1343
Paxton, B., Bildsten, L., Dotter, A., et al. 2011, ApJS, 192, 3
Paxton, B., Cantiello, M., Arras, P., et al. 2013, ApJS, 208, 4
Podsiadlowski, P., Hsu, J. J. L., Joss, P. C., & Ross, R. R. 1993, Nature, 364, 509
Sahu, D. K., Anupama, G. C., & Chakradhari, N. K. 2013, MNRAS, 433, 2
Shetty, R., Vogel, S. N., Ostriker, E. C., & Teuben, P. J. 2007, ApJ, 665, 1138
Shivvers, I., Mazzali, P., Silverman, J. M., et al. 2013, ArXiv e-prints
Spyromilio, J. 1994, MNRAS, 266, L61
Spyromilio, J., Meikle, W. P. S., Learner, R. C. M., & Allen, D. A. 1988, Nature, 334, 327
Stancliffe, R. J. & Eldridge, J. J. 2009, MNRAS, 396, 1699
Stathakis, R. A., Dopita, M. A., Cannon, R. D., & Sadler, E. M. 1991, Supernovae, 649
Suntzeff, N. B. & Bouchet, P. 1990, AJ, 99, 650
Taubenberger, S., Navasardyan, H., Maurer, J. I., et al. 2011, MNRAS, 413, 2140
Tsvetkov, D. Y., Volkov, I. M., Baklanov, P., Blinnikov, S., & Tuchin, O. 2009, Peremennye Zvezdy, 29, 2
Tsvetkov, D. Y., Volkov, I. M., Sorokina, E., et al. 2012, Peremennye Zvezdy, 32, 6
Tully, R. B., Shaya, E. J., Karachentsev, I. D., et al. 2008, ApJ, 676, 184
Van Dyk, S. D., Li, W., Cenko, S. B., et al. 2011, ApJ, 741, L28
Van Dyk, S. D., Zheng, W., Clubb, K. I., et al. 2013, ApJ, 772, L32
Woosley, S. E. & Heger, A. 2007, Phys. Rep., 442, 269
Yaron, O. & Gal-Yam, A. 2012, PASP, 124, 668

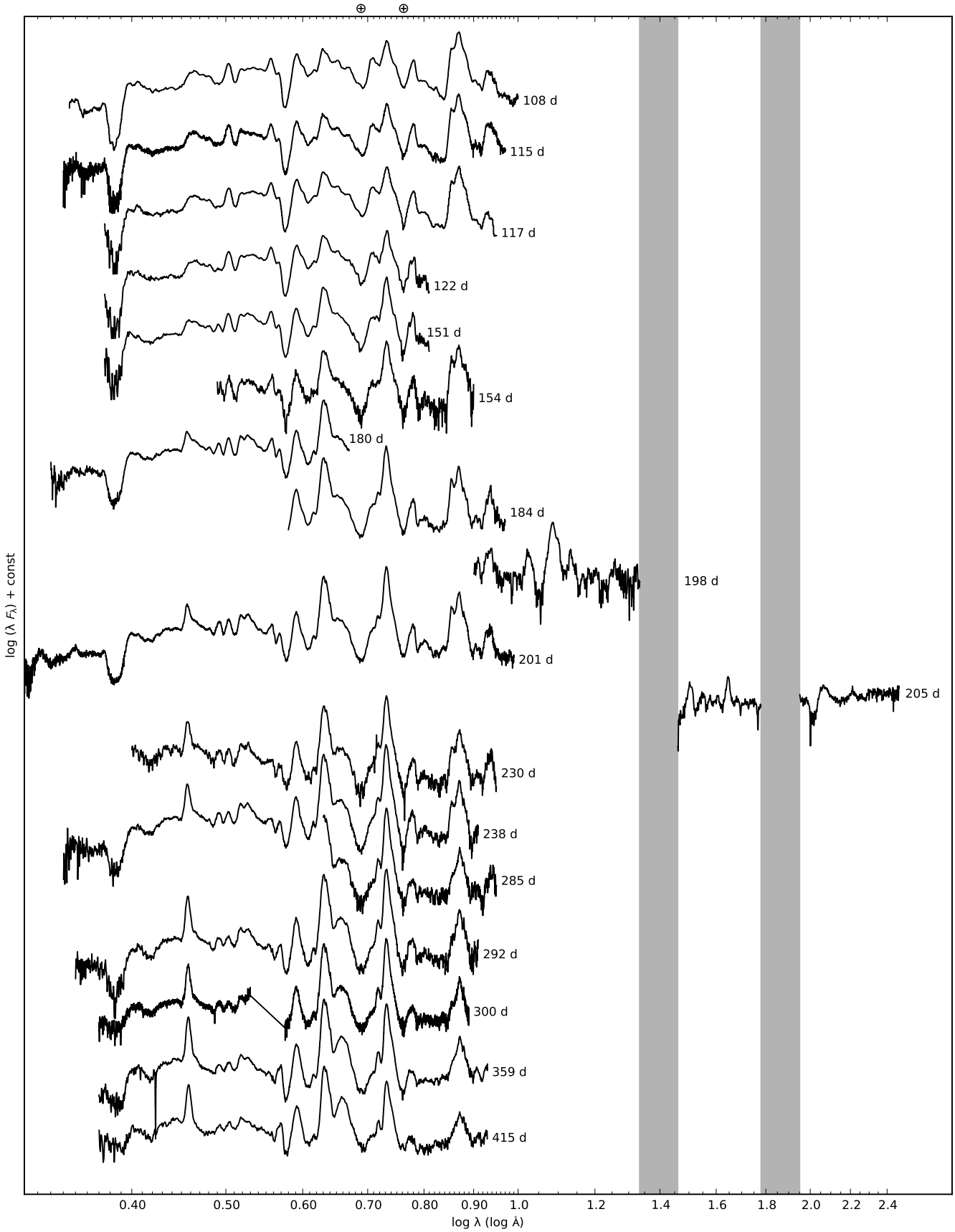

Fig. 7. Sequence of the observed late-time (100−415 days) spectra for SN 2011dh. Spectra obtained on the same night using the same telescope and instrument have been combined and each spectra have been labelled with the phase of the SN. Telluric absorption bands are marked with a ⊕ symbol in the optical and shown as grey regions in the NIR.

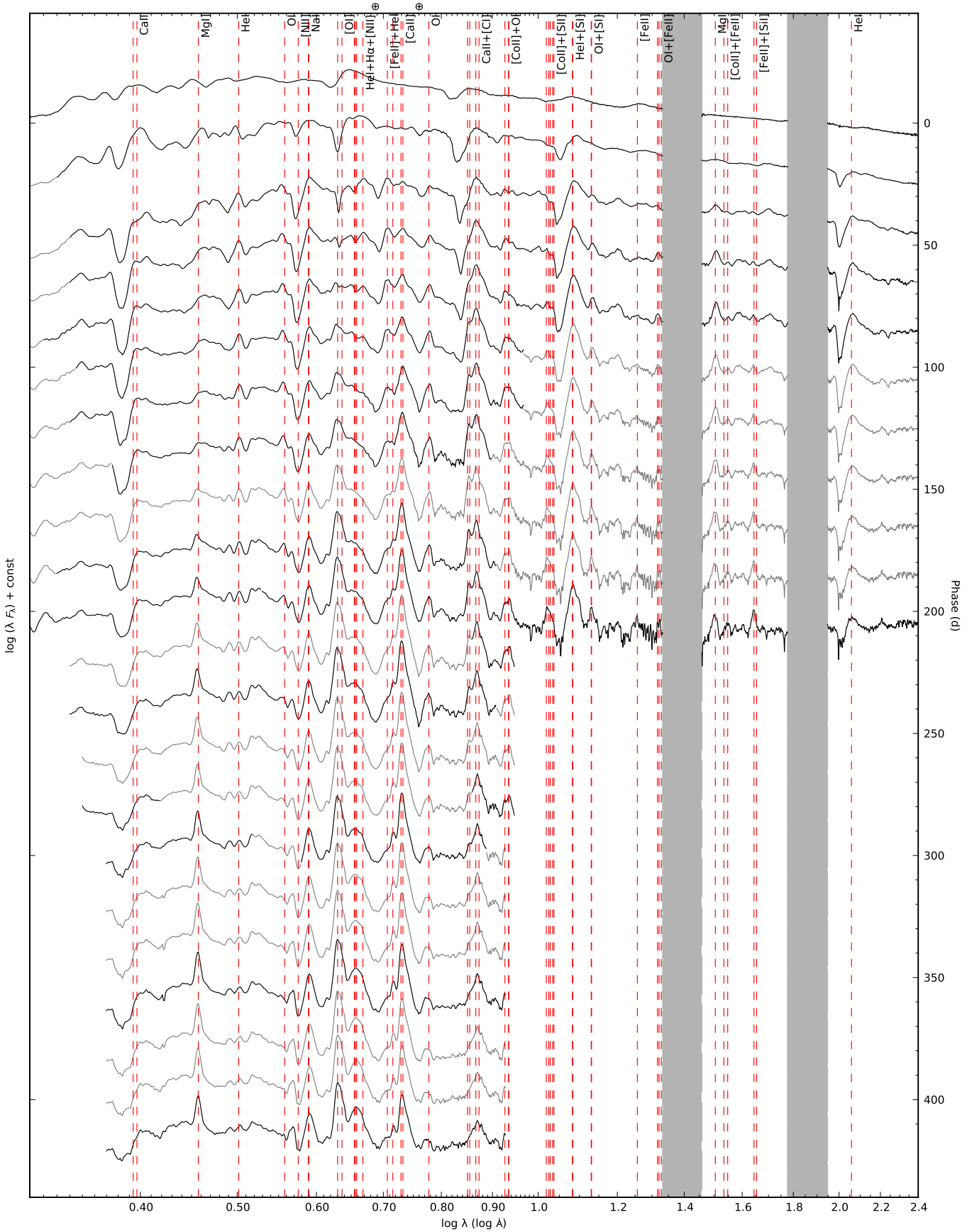

Fig. 8. The 5−425 days optical and NIR (interpolated) spectral evolution for SN 2011dh with a 20-day sampling. Telluric absorption bands are marked with a ⊕ symbol in the optical and shown as grey regions in the NIR.

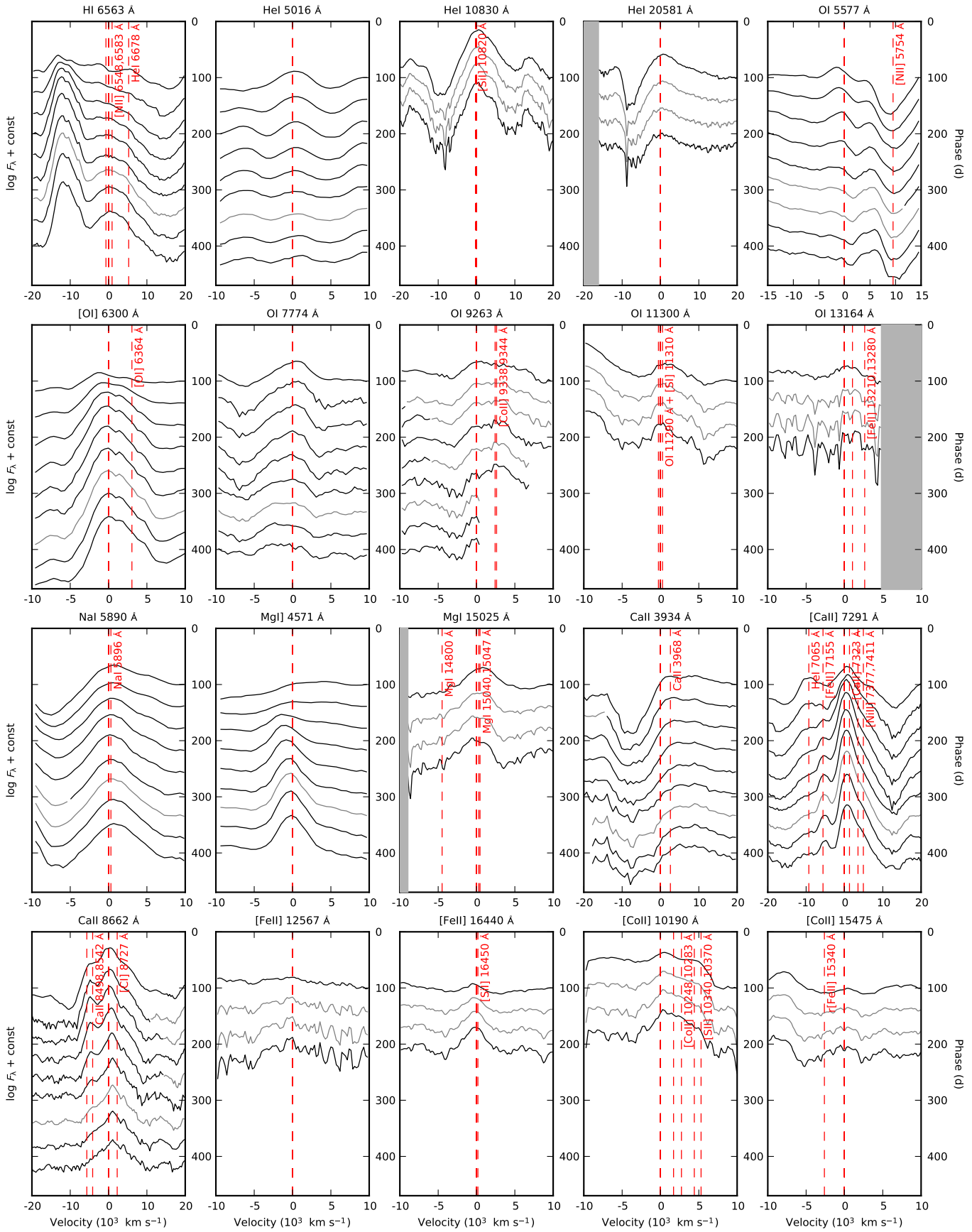

Fig. 9. The >100 days (interpolated) spectral evolution of all identified lines. Multiple or blended lines are marked with red dashed lines and telluric absorption bands in the NIR shown as grey regions.

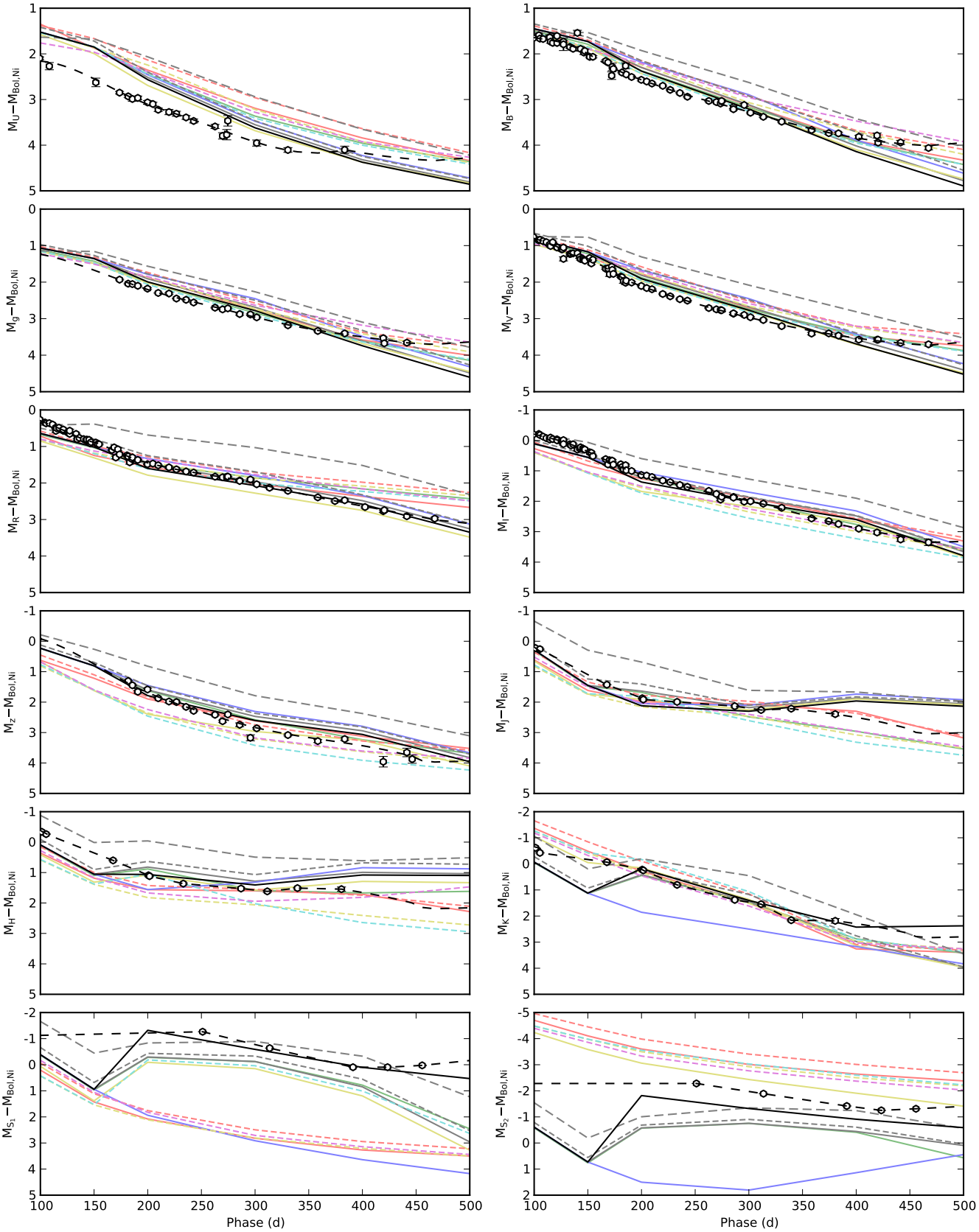

Fig. 17. The 100−500 days observed (black circles) and J14 model optical, NIR and MIR (absolute) magnitudes normalized to the radioactive decay chain luminosity of 0.075 $M_\odot$ of ^{56}Ni. The preferred model (12F) is shown in full colour and all other models in shaded colour. The models are displayed as follows; 12A (red solid line), 12B (green solid line), 12C (black solid line), 12D (yellow solid line), 12E (blue solid line), 12F (black solid line), 13A (red short-dashed line), 13C (yellow short-dashed line), 13D (cyan short-dashed line), 13E (magenta short-dashed line), 13G (black short-dashed line), 17A (black long-dashed line).

Table 4. Late-time (>100 days) optical colour-corrected JC *U* and S-corrected JC *BVRI* magnitudes for SN 2011dh. Errors are given in parentheses.

JD (+2400000) (d)	Phase (d)	*U* (mag)	*B* (mag)	*V* (mag)	*R* (mag)	*I* (mag)	Telescope (Instrument)
55817.35	104.35	...	16.00 0.03	15.20 0.02	14.64 0.02	14.04 0.02	AS-Schmidt (SBIG)
55818.33	105.33	...	16.08 0.02	15.19 0.02	14.68 0.01	14.09 0.01	AS-Schmidt (SBIG)
55821.31	108.31	16.77 0.08	16.12 0.02	15.26 0.01	14.70 0.01	14.17 0.01	CA-2.2m (CAFOS)
55824.32	111.32	...	...	15.31 0.02	14.77 0.03	14.25 0.03	AS-Schmidt (SBIG)
55827.33	114.33	...	16.14 0.03	15.42 0.01	14.88 0.02	14.28 0.01	AS-Schmidt (SBIG)
55827.48	114.48	...	16.15 0.06	15.41 0.03	14.97 0.05	14.32 0.05	AT (ANDOR)
55828.27	115.27	...	16.25 0.03	15.46 0.02	14.91 0.01	14.27 0.01	AT (ANDOR)
55830.28	117.28	...	16.30 0.02	15.38 0.01	14.91 0.01	14.34 0.01	AS-1.82m (AFOSC)
55834.26	121.26	...	16.18 0.03	15.55 0.03	15.03 0.01	14.38 0.02	AT (ANDOR)
55834.31	121.31	...	16.34 0.02	15.56 0.01	15.00 0.02	14.42 0.02	AS-Schmidt (SBIG)
55838.34	125.34	...	...	15.64 0.02	15.12 0.03	14.49 0.01	AS-Schmidt (SBIG)
55839.28	126.28	...	16.37 0.03	15.65 0.02	15.13 0.02	14.52 0.02	AS-Schmidt (SBIG)
55840.26	127.26	...	16.37 0.03	15.62 0.02	15.18 0.02	14.47 0.02	AT (ANDOR)
55840.30	127.30	...	16.42 0.14	15.93 0.06	15.09 0.04	14.60 0.04	AS-Schmidt (SBIG)
55846.26	133.26	...	16.54 0.03	15.85 0.03	15.24 0.02	14.66 0.02	AT (ANDOR)
55847.30	134.30	...	...	15.85 0.03	15.39 0.02	14.71 0.02	AT (ANDOR)
55849.26	136.26	...	16.61 0.04	15.86 0.03	15.38 0.02	14.69 0.02	AT (ANDOR)
55853.27	140.27	...	16.30 0.06	15.90 0.05	15.45 0.05	14.91 0.04	AS-Schmidt (SBIG)
55855.38	142.38	...	...	16.02 0.03	15.50 0.03	14.89 0.03	AT (ANDOR)
55856.24	143.24	...	16.68 0.05	16.08 0.03	15.49 0.02	14.86 0.02	AT (ANDOR)
55858.29	145.29	...	...	16.10 0.03	15.52 0.02	14.92 0.03	AT (ANDOR)
55859.23	146.23	...	16.79 0.04	16.14 0.03	15.62 0.03	14.96 0.03	AT (ANDOR)
55860.22	147.22	...	16.76 0.04	16.17 0.04	15.60 0.02	14.97 0.02	AT (ANDOR)
55864.69	151.69	17.55 0.09	16.94 0.02	16.14 0.01	15.65 0.01	15.10 0.01	AS-1.82m (AFOSC)
55866.28	153.28	...	...	16.30 0.03	15.71 0.02	15.14 0.02	AT (ANDOR)
55867.70	154.70	...	16.97 0.02	16.22 0.03	15.73 0.02	15.26 0.02	CA-2.2m (CAFOS)
55879.66	166.66	...	17.17 0.03	16.58 0.02	16.00 0.02	15.48 0.02	AS-Schmidt (SBIG)
55881.74	168.74	...	17.23 0.02	16.59 0.02	15.95 0.01	15.67 0.03	CA-2.2m (CAFOS)
55883.24	170.24	...	...	16.76 0.06	16.24 0.04	15.55 0.03	AT (ANDOR)
55885.21	172.21	...	17.55 0.08	16.58 0.04	16.04 0.04	15.58 0.03	AT (ANDOR)
55885.73	172.73	...	17.36 0.08	16.67 0.02	...	15.59 0.03	AS-1.82m (AFOSC)
55886.75	173.75	17.99 0.03	17.42 0.01	16.79 0.01	16.19 0.01	15.72 0.01	NOT (ALFOSC)
55893.71	180.71	...	...	16.93 0.02	16.29 0.01	15.78 0.02	AS-Schmidt (SBIG)
55894.76	181.76	18.15 0.02	17.57 0.01	16.96 0.01	16.33 0.01	15.88 0.01	NOT (ALFOSC)
55896.20	183.20	...	...	17.08 0.06	16.50 0.05	15.97 0.04	AT (ANDOR)
55898.19	185.19	...	17.46 0.06	17.14 0.05	16.43 0.04	15.86 0.03	AT (ANDOR)
55898.73	185.73	18.24 0.05	17.65 0.01	17.09 0.01	16.39 0.01	16.03 0.01	NOT (ALFOSC)
55903.76	190.76	18.27 0.04	17.76 0.02	17.19 0.02	16.51 0.02	16.10 0.02	NOT (ALFOSC)
55912.79	199.79	18.46 0.04	17.91 0.02	17.37 0.02	16.72 0.01	16.32 0.01	NOT (ALFOSC)
55917.79	204.79	18.54 0.04	17.99 0.01	17.48 0.01	16.75 0.01	16.39 0.01	NOT (ALFOSC)
55922.76	209.76	18.71 0.04	18.09 0.01	17.56 0.01	16.84 0.01	16.48 0.01	NOT (ALFOSC)
55932.79	219.79	18.86 0.06	18.23 0.01	17.79 0.02	17.00 0.02	16.70 0.02	NOT (ALFOSC)
55939.73	226.73	18.97 0.05	18.39 0.01	17.92 0.02	17.12 0.01	16.82 0.01	NOT (ALFOSC)
55948.73	235.73	19.14 0.04	18.55 0.01	18.09 0.02	17.26 0.01	17.00 0.01	NOT (ALFOSC)
55955.76	242.76	19.28 0.04	18.70 0.01	18.19 0.01	17.36 0.01	17.13 0.01	NOT (ALFOSC)
55975.69	262.69	19.60 0.05	18.98 0.01	18.59 0.01	17.67 0.01	17.45 0.01	NOT (ALFOSC)
55982.74	269.74	19.87 0.07	19.08 0.02	18.69 0.02	17.75 0.01	17.62 0.01	NOT (ALFOSC)
55986.62	273.62	19.88 0.11	19.15 0.03	18.75 0.03	17.78 0.02	17.85 0.03	CA-2.2m (CAFOS)
55987.62	274.62	19.59 0.12	19.10 0.02	18.77 0.02	17.78 0.01	17.76 0.01	LT (RATCam)
55998.66	285.66	...	19.34 0.04	18.97 0.04	18.00 0.02	17.88 0.02	LT (RATCam)
55998.67	285.67	...	19.39 0.02	18.96 0.02	18.01 0.01	17.90 0.01	NOT (ALFOSC)
56008.66	295.66	...	19.39 0.03	19.10 0.03	18.07 0.02	18.13 0.03	LT (RATCam)

Table 5. Continued.

JD (+2400000) (d)	Phase (d)	U (mag)	B (mag)	V (mag)	R (mag)	I (mag)	Telescope (Instrument)
56014.51	301.51	20.34 0.07	19.62 0.01	19.22 0.02	18.25 0.01	18.17 0.01	NOT (ALFOSC)
56026.49	313.49	...	19.83 0.02	19.41 0.02	18.47 0.01	18.37 0.02	NOT (ALFOSC)
56043.59	330.59	20.77 0.05	20.10 0.02	19.75 0.02	18.72 0.01	18.67 0.02	NOT (ALFOSC)
56071.42	358.42	...	20.55 0.02	20.22 0.03	19.17 0.02	19.29 0.03	NOT (ALFOSC)
56087.43	374.43	...	20.78 0.02	20.37 0.03	19.42 0.02	19.54 0.02	NOT (ALFOSC)
56096.48	383.48	21.28 0.08	20.87 0.03	20.52 0.03	19.49 0.02	19.72 0.03	NOT (ALFOSC)
56115.44	402.44	...	21.13 0.03	20.82 0.04	19.86 0.02	20.06 0.04	NOT (ALFOSC)
56132.43	419.43	...	21.27 0.05	20.99 0.05	20.14 0.03	20.35 0.05	NOT (ALFOSC)
56133.40	420.40	...	21.43 0.05	20.99 0.05	20.12 0.03	...	NOT (ALFOSC)
56154.39	441.39	...	21.63 0.04	21.28 0.05	20.49 0.03	20.79 0.06	NOT (ALFOSC)
56180.37	467.37	...	22.01 0.04	21.58 0.05	20.81 0.03	21.14 0.11	NOT (ALFOSC)
56313.73	600.73	...	...	22.44 0.10	...	...	NOT (ALFOSC)
56353.50	640.50	...	...	23.02 0.00	...	22.58 0.00	HST (ACS)
56371.69	658.69	...	23.42 0.32	...	...	...	NOT (ALFOSC)
56397.64	684.64	...	...	23.20 0.20	...	...	NOT (ALFOSC)
56445.43	732.43	...	23.96 0.50	...	...	...	NOT (ALFOSC)

Table 6. Late-time (>100 days) optical colour-corrected SDSS u and S-corrected SDSS $griz$ magnitudes for SN 2011dh. Errors are given in parentheses.

JD (+2400000) (d)	Phase (d)	u (mag)	g (mag)	r (mag)	i (mag)	z (mag)	Telescope (Instrument)
55886.75	173.75	18.76 0.04	16.99 0.01	16.37 0.01	16.14 0.01	...	NOT (ALFOSC)
55894.76	181.76	18.92 0.03	17.18 0.02	16.51 0.01	16.27 0.01	16.29 0.02	NOT (ALFOSC)
55898.73	185.73	19.02 0.04	17.23 0.01	16.58 0.01	16.39 0.01	16.47 0.02	NOT (ALFOSC)
55903.76	190.76	19.13 0.08	17.33 0.02	16.70 0.01	16.45 0.01	16.73 0.04	NOT (ALFOSC)
55912.79	199.79	19.29 0.06	17.49 0.02	16.90 0.01	16.64 0.01	16.74 0.04	NOT (ALFOSC)
55922.77	209.77	19.47 0.02	17.71 0.01	17.03 0.01	16.79 0.01	17.13 0.01	NOT (ALFOSC)
55932.79	219.79	19.62 0.05	17.82 0.02	17.20 0.02	16.96 0.02	17.33 0.04	NOT (ALFOSC)
55939.74	226.74	19.76 0.05	18.03 0.01	17.31 0.01	17.07 0.01	17.42 0.02	NOT (ALFOSC)
55948.73	235.73	19.93 0.03	18.15 0.01	17.45 0.01	17.22 0.01	17.67 0.01	NOT (ALFOSC)
55955.76	242.76	20.08 0.03	18.29 0.01	17.56 0.01	17.34 0.01	17.86 0.02	NOT (ALFOSC)
55975.69	262.69	20.32 0.04	18.63 0.01	17.84 0.01	17.65 0.01	18.19 0.02	NOT (ALFOSC)
55982.74	269.74	20.68 0.06	18.74 0.01	17.94 0.01	17.83 0.01	18.47 0.03	NOT (ALFOSC)
55987.62	274.62	20.49 0.11	18.76 0.01	17.95 0.01	17.94 0.01	18.29 0.03	LT (RATCam)
55998.66	285.66	...	19.02 0.03	18.15 0.02	18.06 0.02	18.74 0.06	LT (RATCam)
56008.66	295.66	...	19.13 0.02	18.22 0.01	18.31 0.03	19.26 0.10	LT (RATCam)
56014.52	301.52	21.08 0.05	19.27 0.01	18.39 0.01	18.41 0.01	19.01 0.02	NOT (ALFOSC)
56043.60	330.60	21.53 0.04	19.77 0.01	18.81 0.01	18.91 0.01	19.51 0.03	NOT (ALFOSC)
56071.43	358.43	...	20.20 0.02	19.23 0.02	19.56 0.03	19.98 0.05	NOT (ALFOSC)
56096.49	383.49	22.07 0.07	20.51 0.02	19.52 0.02	20.00 0.03	20.16 0.05	NOT (ALFOSC)
56132.43	419.43	...	20.99 0.03	20.16 0.02	20.65 0.04	21.25 0.17	NOT (ALFOSC)
56133.41	420.41	...	21.14 0.04	20.13 0.03	20.78 0.05	...	NOT (ALFOSC)
56154.39	441.39	...	21.32 0.04	20.51 0.03	21.10 0.06	21.17 0.14	NOT (ALFOSC)
56159.38	446.38	...	...	...	...	21.43 0.13	NOT (ALFOSC)
56313.75	600.75	...	...	22.46 0.11	...	...	NOT (ALFOSC)
56428.46	715.46	...	...	23.10 0.20	...	...	NOT (ALFOSC)

Table 7. Late-time (>100 days) NIR S-corrected 2MASS JHK magnitudes for SN 2011dh. Errors are given in parentheses.

JD (+2400000) (d)	Phase (d)	J (mag)	H (mag)	K (mag)	Telescope (Instrument)
55814.32	101.32	14.38 0.01	13.80 0.01	13.50 0.01	CA-3.5m (O2000)
55818.36	105.36	14.45 0.02	13.91 0.01	13.74 0.01	NOT (NOTCAM)
55880.72	167.72	16.23 0.01	15.38 0.01	14.70 0.01	CA-3.5m (O2000)
55913.68	200.68	17.00 0.01	16.19 0.02	15.31 0.02	CA-3.5m (O2000)
55914.66	201.66	17.05 0.01	16.23 0.02	15.35 0.02	CA-3.5m (O2000)
55946.13	233.13	17.43 0.02	16.78 0.02	16.21 0.02	UKIRT (WFCAM)
55999.91	286.91	18.10 0.02	17.47 0.02	17.31 0.02	UKIRT (WFCAM)
56024.38	311.38	18.46 0.03	17.80 0.03	17.71 0.04	WHT (LIRIS)
56052.47	339.47	18.69 0.02	17.96 0.02	18.60 0.03	WHT (LIRIS)
56093.48	380.48	19.27 0.06	18.40 0.07	19.02 0.09	WHT (LIRIS)

Table 8. MIR Spitzer S_1 and S_2 magnitudes for SN 2011dh. Errors are given in parentheses.

JD (+2400000) (d)	Phase (d)	S_1 (mag)	S_2 (mag)	Telescope (Instrument)
55964.14	251.14	14.300 0.002	13.280 0.002	SPITZER (IRAC)
56026.63	313.63	15.536 0.007	14.280 0.003	SPITZER (IRAC)
56104.23	391.23	17.025 0.012	15.507 0.005	SPITZER (IRAC)
56136.41	423.41	17.337 0.014	15.988 0.006	SPITZER (IRAC)
56168.69	455.69	17.581 0.014	16.241 0.008	SPITZER (IRAC)
56337.59	624.59	18.517 0.083	17.537 0.056	SPITZER (IRAC)
56360.27	647.27	18.675 0.045	17.663 0.030	SPITZER (IRAC)
56477.83	764.83	18.833 0.047	18.047 0.039	SPITZER (IRAC)
56742.28	1029.28	...	18.506 0.091	SPITZER (IRAC)
56742.30	1029.30	...	18.410 0.075	SPITZER (IRAC)
56771.67	1058.67	18.858 0.077	18.543 0.070	SPITZER (IRAC)
56773.84	1060.84	...	18.364 0.058	SPITZER (IRAC)

Table 9. List of late-time (100−415 days) optical and NIR spectroscopic observations.

JD (+2400000) (d)	Phase (d)	Grism	Range (Å)	Resolution	Resolution (Å)	Telescope (Instrument)
55821.33	108.33	b200	3300-8700	...	12.0	CA-2.2m (CAFOS)
55821.33	108.33	r200	6300-10500	...	12.0	CA-2.2m (CAFOS)
55828.35	115.35	R300B	3200-5300	...	4.1	WHT (ISIS)
55828.35	115.35	R158R	5300-10000	...	7.7	WHT (ISIS)
55830.25	117.25	Grism 4	3500-8450	292	19.9	AS 1.82m (AFOSC)
55830.28	117.28	Grism 2	3720-10200	191	37.6	AS 1.82m (AFOSC)
55835.25	122.25	Grism 4	3500-8450	292	19.9	AS 1.82m (AFOSC)
55864.65	151.65	Grism 4	3500-8450	292	19.9	AS 1.82m (AFOSC)
55867.71	154.71	g200	4900-9900	...	12.0	CA-2.2m (CAFOS)
55893.76	180.76	Grism 3	3200-6700	345	12.4	NOT (ALFOSC)
55897.76	184.76	Grism 5	5000-10250	415	16.8	NOT (ALFOSC)
55911.20	198.20	zJ	8900-15100	700	...	WHT (LIRIS)
55914.70	201.70	R300B	3200-5300	...	8.2	WHT (ISIS)
55914.70	201.70	R158R	5300-10000	...	15.4	WHT (ISIS)
55918.69	205.69	HK	14000-25000	333	...	TNG (NICS)
55941.72	228.72	R150V	4000-9500	...	12.9	INT (IDS)
55942.73	229.73	R150V	4000-9500	...	12.9	INT (IDS)
55944.75	231.75	R150V	4000-9500	...	12.9	INT (IDS)
55951.64	238.64	Grism 4	3200-9100	355	16.2	NOT (ALFOSC)
55998.68	285.68	r200	6300-10500	...	12.0	CA-2.2m (CAFOS)
56002.58	289.58	Grism 4	3200-9100	355	16.2	NOT (ALFOSC)
56005.62	292.62	Grism 4	3200-9100	355	16.2	NOT (ALFOSC)
56006.60	293.60	Grism 4	3200-9100	355	16.2	NOT (ALFOSC)
56013.14	300.14	R600B	3680-5300	...	5.7	WHT (ISIS)
56013.14	300.14	R316R	5756-8850	...	3.0	WHT (ISIS)
56071.56	358.56	R500B	3440-7600	322	15.0	GTC (OSIRIS)
56072.61	359.61	R500R	4800-10000	352	20.8	GTC (OSIRIS)
56128.47	415.47	R300B	3600-7000	270	16.7	GTC (OSIRIS)

Table 10. Pseudo-bolometric 3−400 days UV-to-MIR lightcurve for SN 2011dh calculated from spectroscopic and photometric data with a 1-day sampling between 3 and 50 days and a 5-day sampling between 50 and 400 days. Random errors are given in the first parentheses and systematic lower and upper errors (arising from the distance and extinction) respectively in the second parentheses.

JD (+2400000) (d)	Phase (d)	L (log erg s^{-1})	JD (+2400000) (d)	Phase (d)	L (log erg s^{-1})
55717.00	4.00	41.464 (0.001) (0.098,0.186)	55823.00	110.00	41.244 (0.002) (0.094,0.164)
55718.00	5.00	41.552 (0.001) (0.097,0.181)	55828.00	115.00	41.204 (0.002) (0.094,0.164)
55719.00	6.00	41.653 (0.001) (0.097,0.179)	55833.00	120.00	41.163 (0.002) (0.094,0.164)
55720.00	7.00	41.747 (0.001) (0.097,0.178)	55838.00	125.00	41.121 (0.002) (0.094,0.164)
55721.00	8.00	41.835 (0.001) (0.097,0.178)	55843.00	130.00	41.078 (0.002) (0.094,0.164)
55722.00	9.00	41.909 (0.001) (0.097,0.178)	55848.00	135.00	41.033 (0.002) (0.094,0.165)
55723.00	10.00	41.969 (0.001) (0.097,0.177)	55853.00	140.00	40.990 (0.002) (0.094,0.165)
55724.00	11.00	42.018 (0.001) (0.097,0.176)	55858.00	145.00	40.948 (0.002) (0.094,0.165)
55725.00	12.00	42.057 (0.001) (0.097,0.176)	55863.00	150.00	40.906 (0.002) (0.094,0.165)
55726.00	13.00	42.089 (0.001) (0.096,0.175)	55868.00	155.00	40.863 (0.002) (0.094,0.165)
55727.00	14.00	42.117 (0.001) (0.096,0.174)	55873.00	160.00	40.818 (0.002) (0.094,0.165)
55728.00	15.00	42.142 (0.001) (0.096,0.174)	55878.00	165.00	40.773 (0.002) (0.094,0.164)
55729.00	16.00	42.163 (0.001) (0.096,0.173)	55883.00	170.00	40.728 (0.002) (0.094,0.164)
55730.00	17.00	42.182 (0.001) (0.096,0.173)	55888.00	175.00	40.683 (0.002) (0.094,0.164)
55731.00	18.00	42.197 (0.001) (0.096,0.173)	55893.00	180.00	40.639 (0.001) (0.094,0.164)
55732.00	19.00	42.208 (0.001) (0.096,0.172)	55898.00	185.00	40.597 (0.001) (0.094,0.164)
55733.00	20.00	42.214 (0.001) (0.096,0.172)	55903.00	190.00	40.555 (0.001) (0.094,0.164)
55734.00	21.00	42.215 (0.001) (0.096,0.171)	55908.00	195.00	40.516 (0.001) (0.094,0.164)
55735.00	22.00	42.211 (0.001) (0.095,0.171)	55913.00	200.00	40.477 (0.001) (0.094,0.164)
55736.00	23.00	42.200 (0.001) (0.095,0.170)	55918.00	205.00	40.438 (0.001) (0.094,0.164)
55737.00	24.00	42.184 (0.001) (0.095,0.168)	55923.00	210.00	40.403 (0.001) (0.094,0.164)
55738.00	25.00	42.164 (0.001) (0.095,0.167)	55928.00	215.00	40.368 (0.001) (0.094,0.164)
55739.00	26.00	42.141 (0.001) (0.094,0.166)	55933.00	220.00	40.334 (0.001) (0.094,0.164)
55740.00	27.00	42.116 (0.001) (0.094,0.165)	55938.00	225.00	40.300 (0.001) (0.094,0.164)
55741.00	28.00	42.090 (0.001) (0.094,0.164)	55943.00	230.00	40.267 (0.001) (0.094,0.164)
55742.00	29.00	42.064 (0.001) (0.094,0.163)	55948.00	235.00	40.235 (0.001) (0.094,0.163)
55743.00	30.00	42.039 (0.001) (0.094,0.162)	55953.00	240.00	40.204 (0.001) (0.094,0.163)
55744.00	31.00	42.016 (0.001) (0.093,0.162)	55958.00	245.00	40.172 (0.001) (0.094,0.163)
55745.00	32.00	41.995 (0.001) (0.093,0.161)	55963.00	250.00	40.139 (0.001) (0.094,0.163)
55746.00	33.00	41.976 (0.001) (0.093,0.161)	55968.00	255.00	40.106 (0.001) (0.094,0.163)
55747.00	34.00	41.959 (0.001) (0.093,0.160)	55973.00	260.00	40.072 (0.001) (0.094,0.163)
55748.00	35.00	41.942 (0.001) (0.093,0.160)	55978.00	265.00	40.039 (0.002) (0.094,0.163)
55749.00	36.00	41.927 (0.001) (0.093,0.160)	55983.00	270.00	40.005 (0.002) (0.094,0.163)
55750.00	37.00	41.913 (0.001) (0.093,0.159)	55988.00	275.00	39.972 (0.002) (0.094,0.163)
55751.00	38.00	41.899 (0.001) (0.093,0.159)	55993.00	280.00	39.939 (0.002) (0.094,0.163)
55752.00	39.00	41.885 (0.001) (0.093,0.159)	55998.00	285.00	39.906 (0.002) (0.094,0.163)
55753.00	40.00	41.873 (0.001) (0.093,0.159)	56003.00	290.00	39.872 (0.002) (0.094,0.163)
55754.00	41.00	41.859 (0.001) (0.093,0.159)	56008.00	295.00	39.838 (0.002) (0.094,0.163)
55755.00	42.00	41.846 (0.001) (0.093,0.159)	56013.00	300.00	39.804 (0.002) (0.094,0.163)
55756.00	43.00	41.834 (0.001) (0.093,0.159)	56018.00	305.00	39.770 (0.002) (0.094,0.163)
55757.00	44.00	41.822 (0.002) (0.093,0.159)	56023.00	310.00	39.737 (0.002) (0.094,0.163)
55758.00	45.00	41.811 (0.002) (0.093,0.159)	56028.00	315.00	39.703 (0.002) (0.094,0.163)
55759.00	46.00	41.800 (0.001) (0.093,0.159)	56033.00	320.00	39.670 (0.002) (0.094,0.163)
55760.00	47.00	41.790 (0.001) (0.093,0.159)	56038.00	325.00	39.638 (0.002) (0.094,0.163)
55761.00	48.00	41.781 (0.001) (0.093,0.159)	56043.00	330.00	39.605 (0.002) (0.094,0.163)
55762.00	49.00	41.771 (0.002) (0.093,0.159)	56048.00	335.00	39.572 (0.002) (0.094,0.163)
55763.00	50.00	41.762 (0.002) (0.093,0.159)	56053.00	340.00	39.540 (0.002) (0.094,0.163)
55768.00	55.00	41.715 (0.002) (0.093,0.159)	56058.00	345.00	39.508 (0.002) (0.094,0.163)
55773.00	60.00	41.669 (0.002) (0.093,0.159)	56063.00	350.00	39.476 (0.002) (0.094,0.163)
55778.00	65.00	41.627 (0.002) (0.093,0.160)	56068.00	355.00	39.445 (0.002) (0.094,0.163)
55783.00	70.00	41.585 (0.002) (0.093,0.160)	56073.00	360.00	39.413 (0.002) (0.094,0.163)
55788.00	75.00	41.544 (0.002) (0.093,0.161)	56078.00	365.00	39.382 (0.002) (0.094,0.163)
55793.00	80.00	41.501 (0.002) (0.093,0.162)	56083.00	370.00	39.351 (0.002) (0.094,0.163)
55798.00	85.00	41.458 (0.002) (0.094,0.162)	56088.00	375.00	39.320 (0.002) (0.094,0.163)
55803.00	90.00	41.415 (0.002) (0.094,0.162)	56093.00	380.00	39.289 (0.002) (0.094,0.163)
55808.00	95.00	41.372 (0.002) (0.094,0.163)	56098.00	385.00	39.255 (0.002) (0.094,0.163)
55813.00	100.00	41.330 (0.002) (0.094,0.163)	56103.00	390.00	39.220 (0.002) (0.094,0.163)
55818.00	105.00	41.287 (0.002) (0.094,0.163)	56108.00	395.00	39.186 (0.002) (0.094,0.164)